1 **Revision 1**

2 # Trace element partitioning between anhydrite, sulfate melt and silicate melt

3 Michael C. Hutchinson[1], Richard A. Brooker[2], Jon D. Blundy[3], John H. Dilles[1], Charles T.
4 Lewis[1]

5 [1]College of Earth, Ocean, and Atmospheric Sciences, Oregon State University, Corvallis,
6 Oregon 97331-5501

7 [2]School of Earth Sciences, University of Bristol, Wills Memorial Building, Bristol, United
8 Kingdom, UK, BS8 1RJ

9 [3]Department of Earth Sciences, University of Oxford, South Parks Road, Oxford, United
10 Kingdom, OX1 3AN

11 Corresponding Author - Michael C. Hutchinson (hutchimi@oregonstate.edu)

12 ## Abstract

13 Anhydrite has become increasingly recognized as a primary igneous phase since its discovery
14 in pumices from the 1982 eruption of El Chichon, Mexico. Recent work has provided
15 evidence that immiscible sulfate melts may also be present in high temperature, sulfur-rich,
16 arc magmas. In this study we present partition coefficients for 37 trace elements between
17 anhydrite, sulfate melt and silicate melt based on experiments at 0.2 – 1 GPa, 800 -1200°C
18 and fO_2 > NNO+2.5.

19 Sulfate melt – silicate melt partition coefficients are shown to vary consistently with ionic
20 potential (the ratio of nominal charge to ionic radius, Z / r) and show peaks in compatibility
21 close to the ionic potential of Ca and S. Partition coefficients for many elements, particularly

REE, are more than an order of magnitude lower than previously published data, likely related to differences in silicate melt composition between the studies. Several highly charged cations, including V, W and Mo are somewhat compatible in sulfate melt but are strongly incompatible in anhydrite. Their concentrations in quench material from natural samples may help to fingerprint the original presence of sulfate melt.

Partition coefficients for 2+ and 3+ cations between anhydrite and silicate melt vary primarily as a function of the calcium partition coefficients ($D_{Ca}^{Anh-Sil}$) and can be described in terms of exchange reactions involving the Ca^{2+} site in anhydrite. Trivalent cations are dominantly charge-balanced by Na^{1+}. Most data are well fit using a simple lattice-strain model, although some features of the partitioning data, including $D_{La}^{Anh-Sil} > D_{Ce}^{Anh-Sil}$, suggest the occurrence of two distinct anhydrite Ca-sites with slightly different optimum radii at the experimental conditions.

The ratio $D_{Sr}^{Anh-Sil}$ / $D_{Ca}^{Anh-Sil}$ is shown to be relatively insensitive to silicate melt composition and should vary from 0.63 – 0.53 between 1200 - 800°C, based on a simple, 'one-site' lattice strain model. Comparison to $D_{Sr}^{Anh-Sil}$ and $D_{Ca}^{Anh-Sil}$ calculated for natural anhydrite suggests that in most cases, including the S-rich eruptions of Pinatubo and El Chichon, the composition of anhydrite is consistent with early crystallization of anhydrite close to the liquidus of silicate melt with a composition approximately that of the bulk erupted material. This illustrates how anhydrite (and perhaps sulfate melt) provides a mechanism to transport large quantities of sulfur from significant depth to the eruptive environment.

Keywords

Sulfate melt, arc magmas, anhydrite, trace element partitioning, experimental petrology

Introduction

Primary igneous anhydrite was first identified in pumices from the 1982 eruption of El Chichón, Mexico (Luhr et al. 1984), and has since been identified in a variety of erupted products and intrusive rocks (for review see Luhr 2008). Experimental studies have shown that anhydrite is stable in sulfur-rich magmas under oxidized conditions (fO_2 >NNO+1.5) at temperatures 750-1100°C (Carroll and Rutherford 1987; Luhr 1990; Clemente et al. 2004; Costa et al. 2004; Zajacz et al. 2012; Huang and Keppler 2015; Masotta and Keppler 2015; Matjuschkin et al 2016; Zajacz and Tsay 2019; Li et al 2021) and is progressively replaced by an immiscible sulfate melt over a temperatures interval starting at ~1000 °C (Jugo et al. 2005; Veksler et al. 2012; Hutchinson et al. 2020). However igneous anhydrite and sulfate melts are rarely preserved in the geologic record. Phenocrystic anhydrite may break down during magmatic degassing, as sulfur is removed from the magma (Chambefort et al. 2008), and after cooling below ~200°C it is readily dissolved from solidified rocks by meteoric fluids (Luhr et al. 1984). Sulfate melts are even more challenging to identify in nature and may only exist transiently before converting to anhydrite at lower temperatures (Hutchinson et al. 2020). However, "wormy anhydrite" inclusions, interpreted as trapped sulfate melt, have been reported in amphibole from the San Jose Ignimbrite at Yanacocha, Peru (Chambefort et al. 2008), and anhydrite "droplets" have been described in olivine-hosted multiphase inclusions from Tolbachik volcano in the Kamchatka arc (Kamenetsky et al. 2017).

Anhydrite is an important reservoir for sulfur in many low-temperature, oxidized, arc magmas, and both anhydrite and sulfate melt may play a crucial role in the transport of sulfur through the crust (Streck and Dilles 1998; Chambefort et al. 2008; Hutchinson and Dilles 2019; Hutchinson et al. 2020). Understanding the physical and chemical conditions, as well as the timing, of sulfate saturation in individual systems is therefore critical to assessing the ultimate sources of sulfur to both SO_2-rich volcanic eruptions and to sulfur-rich magmatic hydrothermal ore deposits.

Igneous anhydrite commonly contains measurable concentrations of a number of trace elements including Sr, Fe, P and REE (Chambefort et al. 2008; Xiao et al. 2012; Hutchinson and Dilles 2019), however the interpretation of anhydrite trace element data is limited by a lack of information on the partitioning of these elements between sulfate phases and silicate melt. The only published anhydrite – silicate melt partition coefficients to date (Luhr et al. 1984) are based on instrumental neutron activation analysis (INAA) of anhydrite phenocrysts and interstitial silicate glass from El Chichón pumice. This method relies on the analysis of bulk anhydrite separates (rather than in-situ analysis of crystal rims) and does not necessarily reflect equilibrium partitioning at eruptive conditions. INAA analyses were further complicated by apatite inclusions in anhydrite grains, and apatite-corrected anhydrite compositions have large uncertainties.

Trace element partitioning between immiscible sulfate and silicate melts has been investigated in a single set of centrifuge autoclave experiments at 100 MPa and 900-1000 °C by Veksler et al. (2012). However, the starting composition in these experiments resulted in sulfate melts which were dominated by alkalis (Na_2O, K_2O, Rb_2O and Cs_2O), rather than

CaO, and may not be directly applicable to sulfate melts in natural arc magmas (e.g. Hutchinson et al. 2020).

Here, we present anhydrite – silicate melt and sulfate melt – silicate melt partition coefficients ($D^{Anh\text{-}Sil}$ and $D^{SM\text{-}Sil}$, respectively) based on analysis of phases produced in experiments on sulfate rich trachydacite and trachyandesite compositions at 800-1200 °C and 0.2-1 GPa.

Methods

Experimental methods

Three trachydacite starting compositions (with increasing water content: D1, D2 and D3) and one trachyandesite starting composition (A1) were used (Table 1), based on the compositions of the Luhr Hill porphyritic granite and the McLeod Hill quartz monzodiorite respectively, both from Yerington, NV (Dilles 1987). Starting compositions were doped with trace elements at a level of ~50-100ppm using ICP standard solutions stabilized with HNO_3 which was subsequently driven off as water and NO_2. In order to accurately determine the concentration of trace elements in starting materials for mass balance calculations, aliquots of starting material were fused at ~1500 °C for ~2 hr at 1 atm and drop quenched in water.

Experimental methods are described in detail by Hutchinson et al. (2020) and are summarized here. Experiments were conducted at the University of Bristol using end-loaded piston cylinder apparatus and a gas-pressurized titanium-zirconium molybdenum (TZM) cold seal pressure vessel. Experiments were carried out using $Au_{80}Pd_{20}$ capsules at 0.2-1 GPa and 800-1200 °C. Oxygen fugacity was fixed between NNO +2.7 and NNO +3.8 using a solid redox buffer in a double capsule configuration (piston-cylinder experiments) or using an H_2-Ar pressurizing gas mix (TZM experiments). Experiments were first taken to 1150–1200 °C at

run pressures for ~ 2 h to ensure melting and homogenization of starting materials, then to the final temperature. Run durations were typically 48 hrs for experiments at ≤1100 °C and 4-8 hr for experiments at 1200 °C (Table 2).

Experimental run products (Table 2, Fig.1) included silicate glass, silicate and oxide phases, anhydrite and the quench products of sulfate melt. These quench products (Fig 1a) were complex and difficult to prepare as polished sections but generally consisted of finely intergrown laths of anhydrite with interstitial, alkali-rich material.

Analytical methods

As a result of their complex quench textures, the accurate determination of bulk sulfate melt composition is challenging (see Hutchinson et al. 2020 for details). We have therefore explored a range of analytical techniques, and have compared sulfate melt trace element concentrations using both laser-ablation inductively-coupled-plasma mass-spectrometry (LA-ICP-MS) and secondary ion mass spectrometry (SIMS). For selected trace elements we have also compared these results to mass balance calculations, which are constrained by the more accurate measurements of silicate melt trace element concentrations.

Trace element concentrations in experimentally produced anhydrite were measured by SIMS, and major elements and Sr were also measured by electron probe microanalysis (EPMA). Although experimental anhydrite grains were too small to analyze by LA-ICP-MS, in order to cross-calibrate SIMS and EPMA analyses of anhydrite, a number of natural and synthetic anhydrite standards were analyzed by both SIMS and EPMA and compared to accepted values, previously measured by LA-ICP-MS (Appendix 1). As a result, small, systematic corrections (~10 – 25%) have been applied to SIMS measurements of Sr, Y and Ba and to EPMA measurements of Sr (see Appendix 1).

LA-ICP-MS analyses of fused starting materials, experimental silicate glasses, and sulfate melts were carried out at Texas Tech University using a New Wave UP213 Nd:YAG laser coupled with an Agilent 7500cs ICP-MS. Laser conditions were of 2-2.5 J/cm^2, 5 Hz and 40 μm diameter spot for sulfates and 4 J/cm^2, 10 Hz and 30 μm diameter spot for silicate glass. Basaltic reference glass GSD was used as an external standard, and results were normalized to either ^{29}Si (silicate glass) or ^{43}Ca (sulfate melts, anhydrite) as measured independently by EPMA (Hutchinson et al. 2020).

SIMS analyses of experimental silicate glasses, sulfate melts and anhydrite crystals were carried out at the Edinburgh Ion Microprobe facility (EIMF) using a Cameca ims-4f with a 12-15 nA, $^{16}O^-$ primary beam, net impact energy of 15 keV and spot size of 12-25 μm. Only high energy (120±20 eV) positive secondary ions were measured to reduce the presence of molecular ions. Measurements of rare earth elements (REE) isotopes were corrected for the presence of oxides based on REEO / REE ratios for silicate (values from Hinton 1990) and calcite (for anhydrite and sulfate melt analyses, values from Law et al. 2000). Measured CeO / Ce ratios for anhydrite analyses agreed well with those predicted. Values for F and Cl in anhydrite and sulfate melts are only approximate as ion yields for these elements are strongly affected by matrix composition, and no matrix-matched standard was available.

EPMA analyses of anhydrite grains were carried out at Oregon State University using a Cameca SX-100 with a 10μm diameter beam, 15kV accelerating voltage and a 30nA beam current.

Sulfate melts were analyzed in seven experiments with trachydacite starting materials (D1, D2, D3) and in two experiments with trachyandesite starting material (A1). Anhydrite grains were analyzed by SIMS in six experiments with trachydacite starting material (D2),

representing isothermal (0.2 – 1GPa, 1000 °C) and isobaric series (900 – 1100 °C, 0.75 GPa), and in one experiment with trachyandesite starting material (A1). Anhydrite Sr concentrations were measured by EPMA in 27 experiments including both tranchydacite and trachyandesite starting materials (see Table 2).

Results

Silicate glass trace element composition

The trace element contents of all experimental silicate glasses were measured by LA-ICP-MS. A subset of samples was also analyzed by SIMS and, with the exception of Li and Co, showed good agreement with LA-ICP-MS data (Appendix 1). Silicate glass trace element concentrations vary systematically with temperature and show a range of behavior related to partitioning between silicate glass and other phases that are present (Fig. 2). V and Co act similarly, and their concentrations in the silicate glass fall sharply below 1000 °C owing to their compatibility in biotite (e.g. Villemant 1988; Bea et al. 1994) and ilmenite (e.g. Klemme et al. 2006). Li, Ba, Mo, W, Re and to a lesser extent Rb concentrations in the glass decrease above 1000 °C due to their incorporation into sulfate melt, which is increasingly abundant above 1000 °C. REE, Y, Hf, Nb and Zr concentrations do not change significantly between 800-1200 °C, indicating that bulk partition coefficients are relatively constant over this temperature range. The combined proportion of sulfate phases (sulfate melt + anhydrite) in experiments ranged from 10-16 wt%, making these the most abundant phases in all experiments, after silicate melt. Therefore, the similarity of bulk partition coefficients over the entire experimental temperature range implies similar partitioning behavior between silicate melt and both anhydrite and sulfate melt for these elements.

178 **Sulfate melt – silicate melt partition coefficients**

179 Sulfate melt (SM) – silicate melt (Sil) partition coefficients (D_i^{SM-Sil}) have been calculated
180 based on nine experiments using trachyandesite and trachydacite starting compositions at
181 1100-1200 °C and 0.2-1 GPa (Appendix 2). Given the difficulty in obtaining representative
182 sulfate melt analyses, we measured partition coefficients using both LA-ICP-MS (nine
183 experiments) and SIMS (four experiments), and calculated partition coefficients for a subset
184 of elements using mass balance estimates of sulfate melt composition (six experiments). All
185 measured and calculated compositions are given in Appendix 2, and preferred values for each
186 element are given in Table 3, based on criteria below.

187 Mass balance calculations (see Appendix 3) were performed for all experimental runs that
188 contained only silicate melt and sulfate melt, i.e. all experiments at >1160°C, with the
189 exception of SM-62, which also contained anhydrite. The proportion of each phase was
190 calculated using the bulk sulfur content (based on starting mixture) and the sulfur content of
191 the silicate glass and the sulfate melt as determined by EPMA. The concentration of each
192 element in the bulk starting material was determined by LA-ICP-MS of fused starting
193 material. Further details of mass balance calculations are given in Hutchinson et al. (2020)
194 and in Appendix 3. It should be noted that some loss of siderophile elements from
195 experiments may be expected, due to alloying with the precious metal capsule (e.g. Wang et
196 al. 2020), and that this may lead to artificially high mass balance estimates of sulfate melt
197 trace element concentrations. As such, direct measurements of these elements (either LA-
198 ICP-MS or SIMS) are preferred where possible. In the case of Fe, Hall et al. (2004) show that
199 at 1300-1350°C and fO_2 = FMQ+1, Fe loss to a $Au_{80}Pd_{20}$ capsule is limited to <4% relative

over 24 hr. In our experiments Fe loss is likely lower still, owing to lower temperatures and higher fO_2.

D_i^{SM-Sil} as determined by LA-ICP-MS and SIMS (Fig. 3a) are generally in good agreement, despite large analytical uncertainties. Exceptions to this are values for Co, Li, W and Mo that in some experiments fall well below the 1:1 line. Partition coefficients calculated using mass balance estimates of sulfate melt composition also show good agreement with LA-ICP-MS data (Fig. 3b), with the exception of Li.

The cause of the inconsistency for Co, W and Mo between LA-ICP-MS and SIMS methods is not clear, although it may be related to the larger volume of material sampled by LA-ICP-MS versus SIMS analyses. Sulfate melt quench products are heterogeneous, and it is possible that an unidentified quench phase, highly enriched in these elements, was present at some depth below the sample surface, beyond the limits of SIMS analysis. In this case SIMS analysis would yield lower sulfate melt trace element values compared to LA-ICP-MS, as observed. Considering the heterogenous nature of the sulfate melt quench products and the larger volume of material sampled by LA-ICP-MS compared to SIMS, partition coefficients derived from LA-ICP-MS analysis are considered to be more representative.

For lithium, D_{Li}^{SM-Sil} determined by mass balance for six experiments at 1160 - 1200 °C is approximately constant (D_{Li}^{SM-Sil} 1.9 – 2.6), as might be expected at isothermal conditions, and we consider these values the most reliable. By contrast, D_{Li}^{SM-Sil} values determined by LA-ICP-MS analysis of sulfate melts for the same experiments vary by more than an order of magnitude (D_{Li}^{SM-Sil} 0.56 – 15.7), which we consider a consequence of some unknown analytical artifact.

222 The preferred sulfate melt – silicate melt partition coefficients (Table 3) for 42 elements are
223 presented in figure 4. Values for major elements (Cl, K, Na, Ca, Mn, Mg, Fe, P and S) are
224 taken from EPMA data or mass balance calculations of Hutchinson et al. (2020),

225 whereas values for F, Hf, Ta, Th and U are taken from SIMS analyses, Li values are taken
226 from mass balance calculations, and all other elements are based on LA-ICP-MS. Data show
227 that larger 2+ cations (Ba, Sr and Ca) are strongly partitioned into the sulfate melt as are light
228 REE, F and Cl, although, as noted above, values for F should only be considered estimates.
229 Some highly charged cations (W, Mo, P) that are close in size to S^{6+} are also preferentially
230 partitioned into the sulfate melt. With decreasing ionic radius 1+ cations (Cs, Rb, K, Na, Li)
231 appear to increase in preference for sulfate melt varying from moderately incompatible to
232 moderately compatible. High field strength elements (HFSE, Th, U, Zr, Hf, Nb, Ta) tend to
233 be incompatible in sulfate melt, with the exception of W and Mo.

234 Analytical uncertainty accounts for much of the spread in partition coefficient for a given
235 element, however in many cases the lowest partition coefficient calculated for a particular
236 element belonged to a single trachyandesite experiment at 1200°C. This is consistent with
237 existing studies which show that partition coefficients between mineral phases and silicate
238 melts tend to be higher in more polymerized (higher SiO_2) silicate melts (e.g. Mahood and
239 Hildreth 1983; Nash and Crecraft 1985; Kohn and Schofield 1994)

240 **Anhydrite – silicate melt partition coefficients**

241 Anhydrite trace element concentrations have been measured for seven experiments at 900-
242 1100 °C and 0.2-1 GPa including both trachydacite (D2) and trachyandesite (A1) starting
243 compositions. Anhydrite (Anh) – silicate melt (Sil) partition coefficients ($D_i^{Anh-Sil}$) were

calculated on the basis of silicate glass compositions also measured by SIMS, or in the case of silicate melt major elements, using EPMA data of Hutchinson et al. 2020 (see Table 4, Fig. 5). As expected 2+ and 3+ cations, which are close in size to Ca^{2+} (i.e. Sr and light-middle REE), show a preference for anhydrite ($D_{Sr}^{Anh-Sil}$ ~ 10-40, $D_{La}^{Anh-Sil}$ ~ 2-12, $D_{Gd}^{Anh-Sil}$ ~ 1.5-14) whereas smaller 2+ cations (Mg, Mn) and 1+ cations (Li, Na, K, Rb) strongly favor the silicate melt. Heavier REE (Ho-Lu) are generally somewhat compatible in anhydrite, except in the more mafic trachyandesite experiment. $D_{Sr}^{Anh-Sil}$ values were also calculated for 27 experiments based on EPMA analysis of anhydrite (Appendix 4), and in all cases agree well with values based on SIMS analyses.

Previously published $D_{REE}^{Anh-Sil}$ value, based on instrumental neutron activation analysis (INAA) of anhydrite phenocrysts and matrix glass at El Chichon (Luhr et al. 1984), agree well with the experimental values presented here, and also show greater affinity for light-middle REE than heavy REE in anhydrite (Fig. 5b).

Discussion

Comparison with previous work on sulfate – silicate melt partitioning

Representative sulfate melt – silicate melt partition coefficients from the study of Veksler et al. (2012) have been included in figure 4 for comparison. Although some general features are similar, for example compatibility of large 2+ cations and REE, there are several differences. Most noticeably, the partition coefficients for REE, Sr and to some extent Ba are all significantly higher in the experiments of Veksler et al. (2012) compared to those calculated here. As previously noted, partition coefficients based on our trachyandesite experiment (silicate glass SiO_2 ~ 54 wt%) are lower than all our trachydacite composition experiments (SiO_2 ~ 64-66 wt%). The silicate glass in the Veksler et al. (2012) experiments was in all

cases even more silica rich (SiO_2 ~75 wt%), thus increased polymerization of the silicate melt is likely responsible for the higher partition coefficients.

More puzzling is the apparent disagreement between partition coefficients for HFSE. For example, Veksler et al. (2012) found that Hf and Zr were both compatible in the sulfate melt, whereas in this study they were found to be the least compatible elements. Furthermore Veksler et al. (2012) found that pairs of elements that might be expected to act similarly (for example Nb-Ta, W-Mo) had quite different partitioning behavior. Elements in figure 4 are plotted in order of increasing ionic potential, i.e. the ratio of nominal charge (Z) to ionic radius (r), as this has been shown to be a useful parameter for characterizing the behavior of cations in melts (Hudon and Baker, 2002 and references therein). Our data appear to show peaks in compatibility for elements with ionic potential close to Ca and S, suggesting partitioning is related to the ease with which trace elements are able to replace the major cations in the sulfate melt structure. In contrast to Veksler et al. (2012) our data suggest a steady increase in partition coefficient with increasing Z/r between Hf and S, with the exception of Si and Al which strongly prefer the silicate melt.

Anhydrite lattice strain models

Anhydrite-silicate melt partitioning data for 2+ and 3+ cations show a parabolic relationship on Onuma diagrams (Fig. 5a,b), demonstrating the influence of ionic radius (r_i) on partitioning. These parabolas can be described by the equation:

Eq.1 $$D_i = D_0 exp\left\{-\frac{4\pi E N_A}{RT} \times \left[\frac{r_0(r_i-r_0)^2}{2} + \frac{(r_i-r_0)^3}{3}\right]\right\}$$

(Brice, 1975; Blundy and Wood, 1994) which links D_i to the mechanical strain associated with replacing a cation in the crystal structure (in this case, Ca^{2+}) with another cation of

different ionic radius. The center of the parabola (r_0) represents the optimum cation radius and the maximum of the parabola (D_0) represents the partition coefficient for a (fictive) cation of that radius. The curvature of the parabola is related to the Young's modulus (E) for the site and to absolute temperature (T). Weighted, non-linear, least squares regression has been used to fit Eq.1 to the 2+ and 3+ partitioning data for each experiment, as illustrated in figure 6a,b (run #16, D2, 1050 °C, 1 GPa). Using data from experiments at ≥1000°C, the average calculated E and r_0 for the anhydrite Ca site are 246 ± 28 GPa and 1.173 ± 0.014 Å for 2+ cations, and 400 ± 58 GPa and 1.103 ± 0.005 Å for 3+ cations respectively.

Although the data are fit moderately well by this approach, a number of features are not fully explained. Firstly, all data from this study, as well as those of Luhr et al. 1984 (Fig. 5b) suggest that $D_{La}^{Anh-Sil} > D_{Ce}^{Anh-Sil}$, which cannot be explained by partitioning of REE into a single crystal lattice site with $r_0 \approx r_{Ca}$ (1.12 Å). Furthermore, in all cases the lattice strain model significantly underestimates $D_{Ba}^{Anh-Sil}$ and overestimates $D_{Mn}^{Anh-Sil}$.

The observed pattern of 3+ cation partitioning behavior may be better modelled with two lattice sites of slightly different optimum radii (Fig. 6c,d). The first site (with $r_{0(A)}$, $E_{(A)}$, $D_{0(A)}$) appears to be well expressed in the partitioning data for 3+ cations with a local maximum at $r_{0(A)}$ ~1.09 Å. Since there are no data for 3+ cations beyond r_i = 1.16 Å the size of the second site ($r_{0(B)}$) is less well-determined, although a fit to the data for one experiment (run #16, Fig. 6d) suggests $r_{0(B)}$ ~1.22 Å. Applying the "two-site" model to data for 2+ cations also better replicates $D_{Ba}^{Anh-Sil}$, with slightly larger estimates of optimum radii at $r_{0(A)}$ ~1.12 Å and $r_{0(B)}$ ~1.25 Å.

The proposal here that partitioning data are suggestive of two individual cation sites is at odds with crystallographic studies of anhydrite (Cheng and Zussman 1963; Hawthorne and Ferguson 1975), which suggest only one distinct Ca site with four sets of Ca-O bond lengths between ~2.32 and 2.56 Å. Differential thermal analysis investigation by Rowe et al. (1967) suggested a reversible thermal effect at ~1195 °C attributed to the change from low to high temperature anhydrite (α-anhydrite and β-anhydrite in the notation of Du 2000), however since it was not possible to quench β-anhydrite, no details of its crystal structure are available. Regardless, since all the partition coefficients reported here are for experimental conditions <1200°C the formation of high-T, β-anhydrite is unlikely. High P-T studies have suggested a kinetically sluggish transition for $CaSO_4$ to a monazite-type structure at pressures between 2 – 5 GPa (Stephens 1964; Crichton et al. 2005; Ma et al. 2007; Bradbury and Williams 2009). Since the anhydrite in our experiments is not pure $CaSO_4$, this transition must occur over some P-T range, and the coexistence of monazite-structured $CaSO_4$ (with a slightly larger Ca^{2+} site) with anhydrite may help to explain the observed partitioning behavior. However, this would require this transition to begin at the conditions of our experiments, at pressures as low as 0.2 GPa, well below what has previously been observed.

The mismatch between the observed and expected $D_{Mn}^{Anh-Sil}$ cannot be explained by either one-site, or two-site models and the observed $D_{Mn}^{Anh-Sil}$ remains low relative to $D_{Mg}^{Anh-Sil}$ and $D_{Ca}^{Anh-Sil}$ in both models. One possibility is that Mn shows a greater-than-expected preference for the silicate melt due to the crystal field stabilization energy (CFSE) associated with occupying the anhydrite Ca^{2+} site in VIII-fold coordination. Alternatively, the difference may be attributed to a higher proportion of Mn^{3+} relative to Mn^{2+} in the silicate melt. Previous studies suggest that at the $f(O_2)$ conditions of our experiments (NNO +2.7 to +3.8)

333 the proportion of Mn^{3+} is likely negligible (Schreiber et al. 1994; Stokes et al. 2019), however
334 these data come from silicate melts very different to those in our experiments.

335 **Partitioning of 2+ cations in anhydrite**

336 For either one or two site fits, it is clear that D_0 is closely related to $D_{Ca}^{Anh-Sil}$ (Fig. 5a), and
337 that $D_{Ca}^{Anh-Sil}$ exerts a first-order control on partitioning for 2+ cations. This is consistent
338 with a homovalent exchange reaction involving the anhydrite Ca site. Using a lattice strain
339 model with average calculated values for E and r_0 (246 ± 28 GPa and 1.173 ± 0.014 Å,
340 respectively), it is possible to calculate expected partition coefficients for 2+ cations as a
341 function of $D_{Ca}^{Anh-Sil}$. For example, using equation 1, $D_{Sr}^{Anh-Sil}$ can be calculated as
342 $D_{Sr}^{Anh-Sil} = D_{Ca}^{Anh-Sil} exp\left(-\frac{686.5}{T}\right)$, and the value of $D_{Sr}^{Anh-Sil}$ / $D_{Ca}^{Anh-Sil}$ is expected to vary
343 between 0.63 and 0.53 over the range of temperatures investigated here (1200°C to 800°C).
344 This agrees closely with the majority of $D_{Sr}^{Anh-Sil}$ values calculated based on EPMA data
345 (Fig.7a).

346 Partition coefficients for four lower temperature experiments deviated significantly from the
347 lattice strain model (Fig. 7a), suggesting disequilibrium. We suggest this can be attributed to
348 changes to the CaO content of the melt during the initial crystallization of anhydrite in these
349 experiments. These four experiments are distinguished by their low temperature (800-900°C),
350 and high bulk S contents (all used starting material D2), and therefore experienced the
351 greatest changes to melt CaO content as a result of significant anhydrite crystallization
352 immediately after being brought down to run temperature from the initial homogenization at
353 1150-1200°C. In these experiments the first-formed anhydrite precipitates from a melt with a
354 high CaO content (and correspondingly low $D_{Ca}^{Anh-Sil}$ and $D_{Sr}^{Anh-Sil}$) relative to that of the

final analyzed glass. As CaO is progressively stripped from the melt, values for $D_{Ca}^{Anh-Sil}$ and $D_{Sr}^{Anh-Sil}$ should both increase, with the final values at run conditions represented in the rims of anhydrite grains. Absent significant diffusive re-equilibration, anhydrite cores, however, may represent initial crystallization with low $D_{Sr}^{Anh-Sil}$. In most cases anhydrite grains analyzed were close in size to the EPMA beam diameter (10μm), and analysis of low-Sr cores was therefore unavoidable. Regardless, this issue is unlikely to affect higher temperature experiments (including those >1000°C used to calculate average parameters for the lattice strain model) due to much smaller changes in melt CaO during the experiment, and more rapid re-equilibration of anhydrite grains at higher run temperatures.

Within the range of compositions investigated (~55-65 wt% SiO_2, ~4-8wt% H_2O), our data suggest that silicate melt composition has only a minor influence on partition coefficients (apart from melt CaO content), and that $D_{Ca}^{Anh-Sil}$ exerts a first-order control on the partitioning of Sr, as well as other 2+ cations, between anhydrite and silicate melt. In the case of Sr, due to the similarity in the ionic radius of Sr^{2+} and Ca^{2+}, temperature also has a limited influence on partitioning, at least within the range of typical magmatic temperatures investigated here (1200 – 800°C).

Although Fe was not measured in anhydrite by SIMS, or by EPMA, the lattice strain model can also be used to estimate the expected $D_{Fe^{2+}}^{Anh-Sil}$ as a function of $D_{Ca}^{Anh-Sil}$, based on the effective ionic radius of Fe^{2+} (0.92Å, Fig. 6a). Using the same average values for r_0 and E as above (derived from experiments ≥1000°C), the ratio $D_{Fe^{2+}}^{Anh-Sil}$ / $D_{Ca}^{Anh-Sil}$ is predicted to vary from 0.0096 to 0.0017 between 1200°C and 800°C.

376 **Partitioning of 3+ cations between anhydrite and silicate melt**

377 The incorporation of 3+ cations, principally the REE, in anhydrite is also dependent
378 on $D_{Ca}^{Anh-Sil}$, but requires a coupled substitution mechanism for charge balance. Of the 1+
379 cations measured, only Na and K were present in anhydrite in sufficient concentrations (130-
380 380 ppm and 20-100 ppm, respectively), and figure 8 shows good correlation between Na and
381 ∑REE + Y concentrations. Since the partition coefficient for Na is generally 0.5 – 1 order of
382 magnitude greater than that of K (Fig. 5c), the contribution of K to exchange reactions
383 involving REE should be relatively small, and the substitution of 3+ cations into anhydrite
384 occurs primarily by reactions of the form:

385 Eq.2 $$2Ca_{Anh}^{2+} + i_{Sil}^{3+} + Na_{Sil}^{1+} \leftrightarrow i_{Anh}^{3+} + Na_{Anh}^{1+} + 2Ca_{Sil}^{2+}$$

386 The lattice strain model developed in this study for 3+ cations (with average calculated E and
387 r_0 of 400 ± 58 GPa and 1.103 ± 0.005 Å respectively) can also explain relative differences in
388 the partitioning of heavy and light REE. The lattice strain model predicts the ratio of
389 $D_{Lu}^{Anh-Sil} / D_{La}^{Anh-Sil}$ should vary between 0.08 at 900°C and 0.11 at 1100°C, consistent with
390 our data (Fig. 7b).

391 **Comparison with natural samples**

392 Due to poor preservation in the natural environment and during sample preparation, primary
393 magmatic anhydrite is rarely identified in igneous rocks and is often only preserved as
394 inclusions in other mineral phases (Luhr 2008; Chambefort et al. 2008; Hutchinson and Dilles
395 2019; Li et al. 2021). Trace element analyses of igneous anhydrite are therefore sparse and
396 due to the small size of anhydrite inclusions, are typically limited to those elements which

can be readily measured by EPMA (Ca, S, Sr, Fe and P, Chambefort et al. 2008; Xiao et al. 2012; Hutchinson and Dilles 2019).

To compare natural anhydrite compositions with the lattice strain model developed here, we have calculated the apparent $D_{Sr}^{Anh-Sil}$ and $D_{Ca}^{Anh-Sil}$ for a number of natural samples, based on previous analysis of anhydrite phenocrysts and inclusions, and various estimates of silicate melt composition (Fig. 9). Estimated silicate melt compositions can be broadly split into those deriving from 'Whole Rock' analyses of erupted material, which includes any phenocrysts present and may approximate liquidus silicate melt composition, and 'Quenched Glass' analyses, which are more evolved than 'Whole Rock' (where phenocrysts are present), and represent the composition of the melt at the time of eruption.

El Chichon. Data for El Chichon Volcano are based on samples from the 1982 eruption, analyzed by Luhr et al. (1984). The anhydrite Sr content used is the average of EPMA analyses of phenocrystic anhydrite, the whole rock CaO and Sr concentrations are based on XRF analyses, and quenched glass concentrations are based on EPMA analyses of glass adjacent to phenocrysts. Anhydrite – silicate melt partition coefficients presented by Luhr et al. (1984) are based on the analysis of quenched glass and imply equilibrium between anhydrite and the erupted silicate melt. However, the lattice strain model developed here is more consistent with equilibrium between anhydrite and the less evolved bulk composition of the erupted material as demonstrated in figure 9. Comparing the bulk SO_3 content estimated for El Chichon pumices (1.25 – 2.5 wt%) with the SO_3 content of similar composition andesitic melts in our experiments (composition A1, ~1.4 wt% SO_3 at 1200°C) indicates that anhydrite or sulfate melt or both were likely liquidus phases in these magmas. Although it is not clear if EPMA analyses of anhydrite grains included both cores and rims, the average

420 composition apparently largely reflects anhydrite crystallizing early, from a basaltic-andesite
421 to andesite melt, with limited re-equilibration at lower temperature prior to eruption, in a
422 similar fashion to that described above for our lower temperature experiments.

423 **Pinatubo.** Anhydrite phenocrysts and inclusions in amphibole were analyzed by Chambefort
424 et al. (2008) from the June 15, 1991 eruption of Pinatubo, and partition coefficients have been
425 calculated using both the reconstructed 'parental dacitic melt' and the 'pre-eruptive rhyolitic
426 melt' of Borisova et al. (2006) ('Whole Rock' and 'Quenched Glass' respectively in Fig. 9).
427 As with El Chichon, partition coefficients calculated on the basis of equilibrium with the
428 parental melt agree closely with the lattice strain model, in contrast to those based on the
429 composition of the erupted silicate melt. Again, this is consistent with the S-rich nature of the
430 1991 eruption of Pinatubo and suggests that the measured anhydrite Sr contents largely
431 reflect anhydrite crystallizing early, in equilibrium with the parental dacite, rather than a
432 more evolved residual melt, immediately prior to eruption.

433 **Aucanquilcha.** Data for Aucanquilcha come from amphibole hosted anhydrite inclusions in
434 dacitic volcanic rocks of the Gordo group (whole rock composition from sample AP-07-41,
435 Walker et al. 2013, anhydrite data from Hutchinson and Dilles, 2019). Temperature estimates
436 based on amphibole-plagioclase pairs suggest trapping of anhydrite at 820 - 860°C (Walker et
437 al. 2013). Although no estimate is available for the silicate melt composition at the time of
438 eruption, the calculated partition coefficients based on the whole rock data are again
439 consistent with the lattice strain model.

440 **Yanacocha.** Anhydrite Sr concentrations at Yanacocha are based on the average of anhydrite
441 inclusions in high-Al amphibole from the San Jose Ignimbrite (sample RC6, Chambefort et
442 al. 2008; Longo et al. 2010) and melt Sr concentration is based on whole-rock analyses of the

same sample. Chambefort et al. (2013) argued that these high-Al amphiboles (and their anhydrite inclusions) likely crystallized at near liquidus temperatures from a basaltic-andesite to andesite magma prior to mixing with a more silicic melt and as such we have calculated the partition coefficient for Ca based on the CaO content of the most primitive igneous rocks at Yanacocha (Atazaico Andesites, ~6 wt% CaO, Longo et al. 2010). As with other examples, the ratio of $D_{Sr}^{Anh-Sil}$ / $D_{Ca}^{Anh-Sil}$ agrees closely with the predicted values from the lattice strain model.

Anhydrite inclusions from this sample at Yanacocha commonly displayed 'wormy' textures (Chambefort et al. 2008) and were interpreted as quenched sulfate melts based on their morphology. This study has shown that the partition behavior of Sr and REE (which were also previously measured in Yanacocha anhydrite inclusions) are broadly similar for both anhydrite and sulfate melts, and that Sr and REE concentrations are unlikely to unambiguously distinguish the two. Future analysis of elements including W, Mo and V, which are somewhat compatible in sulfate melts but very incompatible in anhydrite, may help to distinguish quenched sulfate melts from magmatic anhydrite.

Yerington. Finally at Yerington, partition coefficients are based on anhydrite inclusions in apatite, titanite, plagioclase and quartz (Hutchinson and Dilles 2019), from the Luhr Hill Granite ('Porphyritic Granite' of Dilles 1987), and silicate melt concentrations are based on whole rock analysis of the same sample. In this case partition coefficients differ substantially from the lattice strain model, and suggest that in this case, anhydrite did not crystallize from a melt with a composition approximately that of the whole rock. Assuming that the lattice strain model provides a good model for equilibrium crystallization, the analyzed anhydrite likely grew from a melt with either a higher CaO concentration or with a lower Sr

concentration than the whole rock. It is possible that, as at Yanacocha, this anhydrite originally grew from a less evolved melt with higher CaO, although this would imply little to no re-equilibration between anhydrite and silicate melt during further cooling and crystallization, which seems unlikely in plutonic rocks. Alternatively, ongoing crystallization of plagioclase should deplete the melt in Sr relative to CaO, and these anhydrite grains may reflect equilibrium with a late stage, evolved silicate melt, with significantly lower Sr concentration than the whole rock. This would be consistent with the trapping of anhydrite in late-crystallizing phases including titanite and quartz.

Lastly, it is possible that post-entrapment exchange between anhydrite inclusions and their host minerals has led to a decrease in the anhydrite Sr content after initial crystallization (Hutchinson and Dilles 2019), resulting in a lower than expected $D_{Sr}^{Anh-Sil}$. Detailed study of anhydrite inclusions trapped in a variety of phases, as well as the measurement of Sr zoning in magmatic anhydrite grains, may help to address this question.

Anhydrite Fe contents. One feature of pyroxene and amphibole-hosted anhydrite inclusions from several localities is that they typically contain significantly more Fe (0.2 – 0.7 wt% FeO) than apatite-hosted inclusions or phenocrystic anhydrite from the same samples (Chambefort et al. 2008; Hutchinson and Dilles 2019). This has also been attributed to post-entrapment modification, by diffusion of Fe into anhydrite from the host mafic mineral. This is strongly supported by the lattice strain model, which predicts a ratio of $D_{Fe^{2+}}^{Anh-Sil}$ / $D_{Ca}^{Anh-Sil}$ of between 0.0096 and 0.0017 (at 1200°C to 800°C). For a typical andesitic melt (CaO ~6 wt%, FeO ~5 wt%), equilibrium anhydrite should be expected to contain at most ~0.06% FeO (assuming all Fe as FeO), several times less than that measured.

Implications

Trace element partition coefficients presented in this paper provide a framework for understanding the trace element contents of magmatic anhydrite and sulfate melts crystallizing or exsolving from typical arc magmas. Sulfate melt – silicate melt partition coefficients are broadly similar to those for anhydrite – silicate melt, with compatibility of 2+ and 3+ cations close in ionic radius to Ca. However, sulfate melts also incorporate highly charged cations including Mo, W and V that are very incompatible in anhydrite. Concentrations of these elements have not been reported for potential natural examples of trapped sulfate melts, which include 'wormy anhydrite' from Yanacocha (Chambefort et al. 2008) and 'anhydrite droplets' in multiphase, olivine hosted inclusions from Tolbachik Volcano (Kamenetsky et al. 2017). If future work shows that the concentrations of these elements are elevated (relative to what would be expected for anhydrite) this would provide strong geochemical evidence to complement existing textural evidence for the trapping of sulfate melts.

The possibility that the fractionation of mobile sulfate melts may impart a distinctive trace element signature on very sulfur-rich magmas, is unlikely based on the partition coefficients measured in our experiments. The high temperature required to produce sulfate melts (generally >1000°C, Hutchinson et al. 2020) likely restricts their occurrence to very sulfur-rich, andesitic or basaltic melts (for example those studied as melt inclusions at Colima and Augustine (Vigouroux et al. 2008; Zimmer et al. 2010), or to the mantle wedge, where they may separate from supercritical fluids. During cooling from 1200°C - 1000°C the sulfur content of our most mafic experiments dropped from ~1.4 – 0.6 wt% SO_3, equivalent to the loss of ~1.45 wt% sulfate melt. However over most of this temperature range sulfate melt

511 exists in equilibrium with anhydrite and by 1000°C the sulfate melt is almost completely
512 absent. A reasonable estimate of the quantity of sulfate that could be fractionated from a
513 similar system is therefore <1 wt%. Sulfate melt – silicate melt partition coefficients were
514 <10 for all elements in experiments with trachyandesite composition and in more primitive
515 melts they may be smaller still, owing to a less polymerized silicate melt structure. The small
516 mass of sulfate melt that may be fractionated, and relatively small partition coefficients
517 between sulfate and silicate melt, greatly limits the extent to which fractionation of sulfate
518 melt could alter the trace element content of an evolving magma and thereby impart a
519 distinctive signature.

520 We have shown that trace element partitioning between anhydrite and silicate melt can be
521 described well using a lattice strain approach and that by comparing the calculated $D_{Sr}^{Anh-Sil}$
522 and $D_{Ca}^{Anh-Sil}$ for natural igneous anhydrite to the partitioning model developed here, it is
523 possible to assess the likelihood that anhydrite crystallized from a silicate melt of a given
524 composition. We have shown that in most of the cases investigated, anhydrite compositions
525 are consistent with crystallization from a melt of approximately the same composition as the
526 whole rock (i.e. prior to significant crystallization). This is consistent with sulfate saturation
527 occurring at close to liquidus conditions in sulfur-rich magmatic systems like those at El
528 Chichon, Pinatubo and Yanacocha. In contrast, anhydrite inclusions analyzed from Yerington
529 appear to have crystallized from more evolved residual melts, possibly after melt sulfur
530 contents have become sufficiently elevated through crystallization of other silicate phases to
531 attain anhydrite saturation. In other magmatic systems quantifying zonation in individual
532 anhydrite phenocrysts or identifying distinct anhydrite populations may help to determine
533 their ultimate source, for example in cases where there is evidence for magma mixing.

Although it has become clear that arc magmas are more commonly sulfate-saturated than previously thought (Luhr 2008; Chambefort et al. 2008; Hutchinson and Dilles 2019), there has been little work done to directly investigate the conditions and timing of sulfate saturation in many of these magmatic systems. Understanding the relative timing of anhydrite or sulfate melt saturation is critical for assessing the bulk sulfur contents of magmas as they are transported through the crust. This is particularly important for low temperature magmas where the quantity of sulfur present as anhydrite may far exceed that which is dissolved in the accompanying melt (e.g. El Chichon, Luhr et al. 1984). The same is true of intrusive or older volcanic rocks, where the vast majority of magmatic anhydrite is not preserved, and the original quantity of anhydrite is not readily estimated. In these cases, analysis of sparse anhydrite preserved as inclusions in other minerals is one of few ways to investigate the conditions of sulfate saturation, and to estimate the original bulk sulfur contents.

Acknowledgements

Support for this project came from National Science Foundation grant EAR-1624547. Ion probe time was supported by grant IMF608/1016. We would like to express our gratitude to Frank Tepley, Stuart Kearns and Ben Buse for assistance with microprobe analyses, to Richard Hinton and Cristina Talavera for help with SIMS analyses and to Melanie Barnes and Kevin Werts for LA-ICP-MS analyses. We would also like to thank Yuan Li and Ilya Veksler for their careful reviews.

References

Bea, F., Pereira, M.D., and Stroh, A. (1994) Mineral/leucosome trace-element partitioning in a peraluminous migmatite (a laser ablation-ICP-MS study). Chemical Geology, 117, 291–312.

557 Blundy, J., and Wood, B. (1994) Prediction of crystal–melt partition coefficients from elastic
558 moduli. Nature, 372, 452.

559 Borisova, A.Yu., Pichavant, M., Polvé, M., Wiedenbeck, M., Freydier, R., and Candaudap, F.
560 (2006) Trace element geochemistry of the 1991 Mt. Pinatubo silicic melts, Philippines:
561 Implications for ore-forming potential of adakitic magmatism. Geochimica et
562 Cosmochimica Acta, 70, 3702–3716.

563 Bradbury, S.E., and Williams, Q. (2009) X-ray diffraction and infrared spectroscopy of
564 monazite-structured $CaSO_4$ at high pressures: Implications for shocked anhydrite. Journal
565 of Physics and Chemistry of Solids, 70, 134–141.

566 Brice, J.C. (1975) Some thermodynamic aspects of the growth of strained crystals. Journal of
567 Crystal Growth, 28, 249–253.

568 Carroll, M.R., and Rutherford, Malcolm.J. (1987) The Stability of Igneous Anhydrite:
569 Experimental Results and Implications for Sulfur Behavior in the 1982 El Chichon
570 Trachyandesite and Other Evolved Magmas. Journal of Petrology, 28, 781–801.

571 Chambefort, I., Dilles, J.H., and Kent, A.J.R. (2008) Anhydrite-bearing andesite and dacite as
572 a source for sulfur in magmatic-hydrothermal mineral deposits. Geology, 36, 719.

573 Chambefort, I., Dilles, J.H., and Longo, A.A. (2013) Amphibole Geochemistry of the
574 Yanacocha Volcanics, Peru: Evidence for Diverse Sources of Magmatic Volatiles Related
575 to Gold Ores. Journal of Petrology, 54, 1017–1046.

576 Cheng, G.C.H., and Zussman, J. (1963) The crystal structure of anhydrite ($CaSO_4$). Acta
577 Crystallographica, 16, 767–769.

578 Clémente, B., Scaillet, B., and Pichavant, M. (2004) The solubility of sulphur in hydrous
579 rhyolitic melts. Journal of Petrology, 45, 2171–2196.

580 Costa, F., Scaillet, B., and Pichavant, M. (2004) Petrological and experimental constraints on
581 the pre-eruption conditions of Holocene dacite from Volcán San Pedro (36 S, Chilean
582 Andes) and the importance of sulphur in silicic subduction-related magmas. Journal of
583 Petrology, 45, 855–881.

584 Crichton, W.A., Parise, J.B., Antao, S.M., and Grzechnik, A. (2005) Evidence for monazite-,
585 barite-, and $AgMnO_4$ (distorted barite)-type structures of $CaSO_4$ at high pressure and
586 temperature. American Mineralogist, 90, 22–27.

587 Dilles, J.H. (1987) Petrology of the Yerington Batholith, Nevada; evidence for evolution of
588 porphyry copper ore fluids. Economic Geology, 82, 1750–1789.

589 Du, H. (2000) Thermodynamic assessment of the K_2SO_4-Na_2SO_4-$MgSO_4$-$CaSO_4$ system.
590 Journal of phase equilibria, 21, 6.

591 Hall, L.J., Brodie, J., Wood, B.J., and Carroll, M.R. (2004) Iron and water losses from
592 hydrous basalts contained in $Au_{80}Pd_{20}$ capsules at high pressure and temperature.
593 Mineralogical Magazine, 68, 75–81.

594 Hawthorne, F.C., and Ferguson, R.B. (1975) Anhydrous sulphates; II, Refinement of the
595 crystal structure of anhydrite. The Canadian Mineralogist, 13, 289–292.

596 Hinton, R.W. (1990) Ion microprobe trace-element analysis of silicates: Measurement of
597 multi-element glasses. Chemical Geology, 83, 11–25.

598 Huang, R., and Keppler, H. (2015) Anhydrite stability and the effect of Ca on the behavior of
599 sulfur in felsic magmas. American Mineralogist, 100, 257–266.

600 Hudon, P., and Baker, D.R. (2002) The nature of phase separation in binary oxide melts and
601 glasses. I. Silicate systems. Journal of Non-Crystalline Solids, 303, 299–345.

602 Hutchinson, M.C., and Dilles, J.H. (2019) Evidence for Magmatic Anhydrite in Porphyry
603 Copper Intrusions. Economic Geology, 114, 143–152.

604 Hutchinson, M.C., Brooker, R.A., Dilles, J.H., and Blundy, J. (2020) The stability and
605 composition of sulfate melts in arc magmas. Contributions to Mineralogy and Petrology,
606 175, 92.

607 Jugo, P.J., Luth, R.W., and Richards, J.P. (2005) An experimental study of the sulfur content
608 in basaltic melts saturated with immiscible sulfide or sulfate liquids at 1300° C and 1·0
609 GPa. Journal of Petrology, 46, 783–798.

610 Kamenetsky, V.S., Zelenski, M., Gurenko, A., Portnyagin, M., Ehrig, K., Kamenetsky, M.,
611 Churikova, T., and Feig, S. (2017) Silicate-sulfide liquid immiscibility in modern arc basalt
612 (Tolbachik volcano, Kamchatka): Part II. Composition, liquidus assemblage and
613 fractionation of the silicate melt. Chemical Geology, 471, 92–110.

614 Klemme, S., Günther, D., Hametner, K., Prowatke, S., and Zack, T. (2006) The partitioning
615 of trace elements between ilmenite, ulvospinel, armalcolite and silicate melts with
616 implications for the early differentiation of the moon. Chemical Geology, 234, 251–263.

617 Kohn, S.C., and Schofield, P.F. (1994) The importance of melt composition in controlling
618 trace-element behaviour: an experimental study of Mn and Zn partitioning between
619 forsterite and silicate melts. Chemical Geology, 117, 73–87.

620 Law, K.M., Blundy, J.D., Wood, B.J., and Ragnarsdottir, K.V. (2000) Trace element
621 partitioning between wollastonite and silicate-carbonate melt. Mineralogical Magazine, 64,
622 651–661.

623 Li, H., Zhang, L., Bao, X., Wykes, J.L., Liu, X. (2021) High sulfur solubility in subducted
624 sediment melt under both reduced and oxidized conditions: With implications for S
625 recycling in subduction zones settings. Geochimica et Cosmochimica Acta, 304, 305-326

626 Li, J.-X., Li, G.-M., Evans, N.J., Zhao, J.-X., Qin, K.-Z., and Xie, J. (2021) Primary fluid
627 exsolution in porphyry copper systems: evidence from magmatic apatite and anhydrite
628 inclusions in zircon. Mineralium Deposita, 56, 407–415.

629 Longo, A.A., Dilles, J.H., Grunder, A.L., and Duncan, R. (2010) Evolution of Calc-Alkaline
630 Volcanism and Associated Hydrothermal Gold Deposits at Yanacocha, Peru. Economic
631 Geology, 105, 1191–1241.

632 Luhr, J.F. (1990) Experimental phase relations of water-and sulfur-saturated arc magmas and
633 the 1982 eruptions of El Chichón volcano. Journal of Petrology, 31, 1071–1114.

634 Luhr, J.F. (2008) Primary igneous anhydrite: Progress since its recognition in the 1982 El
635 Chichón trachyandesite. Journal of Volcanology and Geothermal Research, 175, 394–407.

636 Luhr, J.F., Carmichael, I.S.E., and Varekamp, J.C. (1984) The 1982 eruptions of El Chichón
637 Volcano, Chiapas, Mexico: Mineralogy and petrology of the anhydrite bearing pumices.
638 Journal of Volcanology and Geothermal Research, 23, 69–108.

639 Ma, Y.M., Zhou, Q., He, Z., Li, F.F., Yang, K.F., Cui, Q.L., and Zou, G.T. (2007) High-
640 pressure and high-temperature study of the phase transition in anhydrite. Journal of
641 Physics: Condensed Matter, 19, 425221.

642 Mahood, G., and Hildreth, W. (1983) Large partition coefficients for trace elements in high-
643 silica rhyolites. Geochimica et Cosmochimica Acta, 47, 11–30.

644 Masotta, M., and Keppler, H. (2015) Anhydrite solubility in differentiated arc magmas.
645 Geochimica et Cosmochimica Acta, 158, 79–102.

646 Nash, W.P., and Crecraft, H.R. (1985) Partition coefficients for trace elements in silicic
647 magmas. Geochimica et Cosmochimica Acta, 49, 2309–2322.

648 Rowe, J.J., Morey, G.W., and Silber, C.C. (1967) The ternary system K_2SO_4-$MgSO_4$-$CaSO_4$.
649 Journal of Inorganic and Nuclear Chemistry, 29, 925–942.

650 Schreiber, H.D., Kochanowski, B.K., Schreiber, C.W., Morgan, A.B., Coolbaugh, M.T., and
651 Dunlap, T.G. (1994) Compositional dependence of redox equilibria in sodium silicate
652 glasses. Journal of Non-Crystalline Solids, 177, 340–346.

653 Shannon, R.D. (1976) Revised effective ionic radii and systematic studies of interatomic
654 distances in halides and chalcogenides. Acta Crystallographica Section A, 32, 751–767

655 Stephens, D.R. (1964) The hydrostatic compression of eight rocks. Journal of Geophysical
656 Research, 69, 2967–2978.

657 Stokes, T.N., Bromiley, G.D., Potts, N.J., Saunders, K.E., and Miles, A.J. (2019) The effect
658 of melt composition and oxygen fugacity on manganese partitioning between apatite and
659 silicate melt. Chemical Geology, 506, 162–174.

660 Streck, M.J., and Dilles, J.H. (1998) Sulfur evolution of oxidized arc magmas as recorded in
661 apatite from a porphyry copper batholith. Geology, 26, 523.

662 Veksler, I.V., Dorfman, A.M., Dulski, P., Kamenetsky, V.S., Danyushevsky, L.V., Jeffries,
663 T., and Dingwell, D.B. (2012) Partitioning of elements between silicate melt and
664 immiscible fluoride, chloride, carbonate, phosphate and sulfate melts, with implications to
665 the origin of natrocarbonatite. Geochimica et Cosmochimica Acta, 79, 20–40.

666 Vigouroux, N., Wallace, P.J., and Kent, A.J.R. (2008) Volatiles in High-K Magmas from the
667 Western Trans-Mexican Volcanic Belt: Evidence for Fluid Fluxing and Extreme
668 Enrichment of the Mantle Wedge by Subduction Processes. Journal of Petrology, 49,
669 1589–1618.

670 Villemant, B. (1988) Trace element evolution in the Phlegrean Fields (Central Italy):
671 fractional crystallization and selective enrichment. Contributions to Mineralogy and
672 Petrology, 98, 169–183.

673 Walker, B.A., Klemetti, E.W., Grunder, A.L., Dilles, J.H., Tepley, F.J., and Giles, D. (2013)
674 Crystal reaming during the assembly, maturation, and waning of an eleven-million-year
675 crustal magma cycle: thermobarometry of the Aucanquilcha Volcanic Cluster.
676 Contributions to Mineralogy and Petrology, 165, 663–682.

677 Wang, J., Xiong, X., Zhang, L., and Takahashi, E. (2020) Element loss to platinum capsules
678 in high temperature pressure experiments. American Mineralogist 105, 1593–1597.

679 Xiao, B., Qin, K., Li, G., Li, J., Xia, D., Chen, L., and Zhao, J. (2012) Highly Oxidized
680 Magma and Fluid Evolution of Miocene Qulong Giant Porphyry Cu-Mo Deposit, Southern
681 Tibet, China. Resource Geology, 62, 4–18.

682 Zajacz, Z., and Tsay, A. (2019) An accurate model to predict sulfur concentration at
683 anhydrite saturation in silicate melts. Geochimica et Cosmochimica Acta, 261, 288–304.

684 Zajacz, Z., Candela, P.A., Piccoli, P.M., and Sanchez-Valle, C. (2012) The partitioning of
685 sulfur and chlorine between andesite melts and magmatic volatiles and the exchange
686 coefficients of major cations. Geochimica et Cosmochimica Acta, 89, 81–101.

687 Zimmer, M.M., Plank, T., Hauri, E.H., Yogodzinski, G.M., Stelling, P., Larsen, J., Singer, B.,
688 Jicha, B., Mandeville, C., and Nye, C.J. (2010) The Role of Water in Generating the Calc-
689 alkaline Trend: New Volatile Data for Aleutian Magmas and a New Tholeiitic Index.
690 Journal of Petrology, 51, 2411–2444.

691

692 **Figure Captions**

693 **Figure 1.** SEM BSE images of experimental run products. SM – Sulfate Melt, Cap –
694 $Au_{80}Pd_{20}$ capsule, Anhy – Anhydrite, Ilm – Ilmenite, Bt – Biotite. (a) Typical high
695 temperature experiment with heterogenous sulfate melt quench products wetting capsule
696 wall. (b) Typical lower temperature experiment with anhydrite stable alongside biotite and
697 ilmenite.

698 **Figure 2.** Variation in silicate glass trace element concentrations with temperature. Grey bar
699 indicates the concentrations in the bulk starting material for the elements shown. Depletion in
700 Ba at high temperature reflects its compatibility in sulfate melt which was present in

701 experiments ≥1000°C. Depletion of La at all temperatures indicates La compatibility in both
702 anhydrite and sulfate melt, whereas Lu concentrations approximately equal to the bulk
703 concentration indicate partition coefficients of ~1 between anhydrite or sulfate melt and
704 silicate melt. Depletion of V at low temperature likely reflects compatibility in both biotite
705 and ilmenite. Uncertainties are 1s.d. based on repeat analysis of glass.

706 **Figure 3.** Comparison of sulfate melt – silicate melt partition coefficients measured and
707 calculated by different methods. (a) LA-ICP-MS vs SIMS partition coefficients. (b) LA-ICP-
708 MS vs mass balance calculations. Uncertainties are propagated 1 s.d. based on repeat analysis
709 of silicate melt and sulfate melt.

710 **Figure 4.** Sulfate melt – Silicate melt partition coefficients based on analytical methods given
711 in Table 3. Data for Cl, K, Na, Ca, Mn, Mg, Fe, P, S are from Hutchinson et al. (2020). Black
712 crosses indicate experimental data from Veksler et al. 2012 for an alkali-rich system.
713 Elements are arranged by ionic potential (Z / r) with r values taken from Shannon (1976)
714 based on a coordination number (CN) of 6. Elements with varying valence state are plotted as
715 follows: Mn^{2+}, Fe^{2+}, Eu^{3+}, Co^{2+}, V^{5+}, W^{6+}, Mo^{6+}.

716 **Figure 5.** Anhydrite – silicate melt partition coefficients for 2+ (a), 3+ (b) and 1+ (c) cations
717 as a function of effective ionic radius. Partition coefficients are based on EPMA (Mg, Mn,
718 Na, K) or SIMS analysis of silicate glass and SIMS analysis of anhydrite. Uncertainties are 1
719 s.d.. Data from Luhr et al. (1984) are based on INAA of anhydrite crystals and interstitial
720 glass from the 1982 eruption of El Chichon.

721 **Figure 6.** Lattice strain models illustrating "1-site" (a,b) and "2-site" (c,d) fits to partitioning
722 data. Effective ionic radii taken from Shannon (1976) based on a coordination number of 8.

Partition coefficients for Mn and Eu were omitted from parabola fitting. Note that "1-site" fits to data underestimate Ba partition coefficients by approximately an order of magnitude and fail to explain the increase in partition coefficient between Ce and La.

Figure 7. Comparison of experimental partition coefficients with a lattice strain model (LSM) based on average values for E and r_0 (see text). Except for four experiments, the measured ratios of $D_{Sr}^{Anh-Sil}$ / $D_{Ca}^{Anh-Sil}$ (a) all agree closely with those predicted (0.63 - 0.53 at 1200 - 800°C) by the model. Four anomalous points in a) are likely a result of changes to melt CaO content during anhydrite crystallization, and lack of sufficient re-equilibration between early-grown anhydrite and silicate melt in low temperature experiments. Ratios of $D_{Lu}^{Anh-Sil}$ / $D_{La}^{Anh-Sil}$ also agree closely with the lattice strain model (b). Uncertainties are 1 s.d.

Figure 8. Comparison of Na and 3+ cation concentrations in anhydrite on the basis of atoms per formula unit (apfu). Close fit to the 1:1 line suggests that the incorporation of REE^{3+} and Y^{3+} into the anhydrite crystal structure is principally charged balanced by Na^{1+}.

Figure 9. Comparison of partition coefficients calculated for natural samples with those predicted by the lattice strain model (LSM). Anhydrite Sr values are averages based on analyses of anhydrite phenocrysts and inclusions (Chambefort et al. 2008; Hutchinson and Dilles 2019). Silicate melt compositions are based on previously published whole rock or erupted glass compositions (see text for details).

		Starting Material			
		D1	D2	D3	A1
Majors (wt%)	SiO_2	56.87	54.95	55.20	46.34
	TiO_2	0.38	0.35	0.34	0.76
	Al_2O_3	13.18	12.77	12.72	13.94
	FeO	1.03	1.01	1.00	2.34
	Fe_2O_3	1.03	1.01	1.00	2.34
	MnO	0.04	0.03	0.04	0.08
	MgO	0.94	0.92	0.94	2.22
	CaO	6.09	5.99	5.99	8.28
	Na_2O	4.27	4.14	4.06	4.53
	K_2O	4.49	4.38	3.93	3.14
	P_2O_5	0.13	0.14	0.14	0.44
	SO_3	7.73	8.87	7.27	9.16
	Cl	0.02	0.27	0.27	0.01
	H_2O[a]	3.47	4.89	6.80	6.51
Traces (ppm)	Li	83	63	62	60
	Sc	101	73	86	86
	V	87	82	79	108
	Co	111	79	87	107
	Ni	236	108	91	127
	Cu	72	61	52	92
	Rb	85	60	55	43
	Sr	269	251	227	279
	Y	98	73	79	89
	Zr	105	70	73	90
	Nb	106	86	77	92
	Mo	49	27	34	24
	Sn	53	39	42	66
	Cs	90	55	53	26
	Ba	96	81	79	104
	La	104	70	75	85
	Ce	103	68	76	137
	Pr	98	64	68	88
	Nd	98	68	74	92
	Sm	98	66	73	89
	Eu	95	68	71	86
	Gd	95	66	76	85
	Ho	96	65	71	78
	Yb	95	68	74	82
	Lu	91	67	73	79
	Hf	93	68	73	86
	W	72	42	43	55

[a] Bulk H_2O contents are based on measured H_2O contents of silicate glasses in experiments and are subject to an average uncertainty of ±1.15wt%

Run #	Temperature, °C	Pressure, Gpa	Run Duration, hr	$f(O_2)$ (ΔNNO)[a]
"D3" Starting Material				
70	1200	1	4	3.34
42	1100	1	48	3.47
26	1000	1	48	3.46
35	900	1	48	3.56
28	800	1	48	3.63
71	1200	0.75	4	3.51
80	1100	0.75	48	3.61
59	1000	0.75	48	3.58
40	900	0.75	48	3.73
41	800	0.75	48	3.78
56	1000	0.2	46	3.73
47	900	0.2	46	3.81
"D2" Starting Material				
87	1200	1	4.5	3.11
81	1100	1	48	3.37
61	1000	1	48	3.32
18	900	1	48	3.31
19	800	1	48	3.46
57	1200	0.75	8	3.21
69	1100	0.75	48	3.27
16	1050	0.75	48	3.33
24	1000	0.75	48	3.41
68	900	0.75	96	3.39
85	800	0.75	48	3.39
32	1160	0.2	8	3.75
54	1000	0.2	46	3.69
45	900	0.2	46	3.81
"D1" Starting Material				
62	1200	1	8	2.72
63	1100	1	48	2.85
83	1000	1	48	3.20
82	900	1	48	3.15
"A1" Starting Material				
23	1200	1	24	3.25
22	1100	1	48	3.22
21	1000	1	48	3.38

Gl = glass representing quenched silicate melt, SM = quenched sulfate melt, Anh =
Sp = spinel, generally magnetite (Mag) but an Fe-Mg-Al-Cr spinel was also observe

[a]Calculated relative to buffering assemblage as $\Delta \log fO_2 = 2 \log a_{H2O}^{sample}$

[b]Presence of sulfate melt implied by silicate melt composition (see Hutchinson et al

Run Products	$D^{Anh\text{-}Sil}$	$D_{Sr}^{Anh\text{-}Sil}$	$D^{SM\text{-}Sil}$
Gl + SM			X
Gl + SM + Anh		X	
Gl + Anh + Sp + Ilm		X	
Gl + Anh + Bt + Ilm		X	
Gl + Anh + Bt + Ilm		X	
Gl + SM			X
Gl + SM + Anh		X	
Gl + SM^{b} + Anh + Sp		X	
Gl + Anh + Bt + Ilm		X	
Gl + Anh + Bt + Ilm		X	
Gl + SM + Anh + Sp + Ilm		X	
Gl + SM^{b} + Anh + Amph + Sp + Ilm		X	
Gl + SM			X
Gl + SM + Anh		X	
Gl + SM^{b} + Anh + Ilm	X	X	
Gl + Anh + Bt + Ilm		X	
Gl + Anh + Bt + Ilm		X	
Gl + SM			X
Gl + SM + Anh + Sp	X	X	X
Gl + SM + Anh	X	X	
Gl + SM + Anh + Ilm	X	X	
Gl + SM + Anh + Bt + Ilm	X	X	
Gl + Anh + Bt + Ilm		X	
Gl + SM			X
Gl + SM + Anh + Sp + Ilm	X	X	
Gl + SM + Anh + Bt + Sp + Ilm		X	
Gl + SM + Anh		X	X
Gl + SM^{b} + Anh		X	
Gl + SM^{b} + Anh + Bt + Ilm		X	
Gl + Anh + Bt + Amph + Ilm		X	
Gl + SM			X
Gl + SM + Anh + Sp + Ilm	X	X	X
Gl + Anh + Bt + Sp + Ilm		X	

anhydrite, Bt = biotite, Amph = amphibole, Ilm = ilmenit

ec

. 2020)

This is the peer-reviewed, final accepted version for American Mineralogist, published by the Mineralogical Society of America.
The published version is subject to change. Cite as Authors (Year) Title. American Mineralogist, in press.
DOI: https://doi.org/10.2138/am-2022-8345. http://www.minsocam.org/

	Run #			70
	Starting Composition			D3
	Temperature (°C)			1200
	Pressure (GPa)			1
	Sil Method	SM Method	Sil (ppm)	SM (ppm)
Li	LA-ICP-MS	Mass Balance	52.5 (1.4)	135 (21)
F	SIMS	SIMS[a]		
Na	EPMA	Mass Balance	25720 (890)	63000 (15000)
Mg	EPMA	Mass Balance	4540 (170)	14300 (2800)
Al	EPMA	EPMA	78050 (680)	1060 (610)
Si	EPMA	EPMA	297900 (1800)	4300 (1900)
P	EPMA	Mass Balance	400 (110)	2100 (1600)
S	EPMA	Mass Balance	3153 (31)	226000 (19000)
Cl	EPMA	Mass Balance	1295 (33)	13490 (880)
K	EPMA	Mass Balance	30490 (590)	49000 (11000)
Ca	EPMA	Mass Balance	20930 (260)	206000 (12000)
Sc	LA-ICP-MS	LA-ICP-MS	92.1 (1.7)	58 (27)
Ti	LA-ICP-MS	LA-ICP-MS	2280 (34)	520 (160)
Mn	EPMA	EPMA	81.2 (1.8)	140 (86)
Fe	EPMA	Mass Balance	540 (240)	1700 (1200)
V	LA-ICP-MS	LA-ICP-MS	16370 (610)	9300 (9500)
Co	LA-ICP-MS	LA-ICP-MS	76.8 (1.4)	220 (150)
Rb	LA-ICP-MS	LA-ICP-MS	60.9 (2.0)	100 (130)
Sr	LA-ICP-MS	LA-ICP-MS	100.4 (3.2)	1610 (340)
Y	LA-ICP-MS	LA-ICP-MS	67.6 (2.8)	127 (48)
Zr	LA-ICP-MS	LA-ICP-MS	78.3 (2.9)	3.8 (2.1)
Nb	LA-ICP-MS	LA-ICP-MS	84.3 (1.9)	25 (11)
Mo	LA-ICP-MS	LA-ICP-MS	51.8 (2.6)	690 (600)
Cs	LA-ICP-MS	LA-ICP-MS	66.0 (2.5)	42 (41)
Ba	LA-ICP-MS	LA-ICP-MS	37.8 (2.7)	600 (460)
La	LA-ICP-MS	LA-ICP-MS	48.5 (1.7)	310 (100)
Ce	LA-ICP-MS	LA-ICP-MS	55.0 (1.1)	251 (84)
Pr	LA-ICP-MS	LA-ICP-MS	51.47 (94)	213 (61)
Nd	LA-ICP-MS	LA-ICP-MS	53.9 (1.7)	166 (60)
Sm	LA-ICP-MS	LA-ICP-MS	57.7 (2.6)	136 (47)
Eu	LA-ICP-MS	LA-ICP-MS	55.0 (1.4)	159 (53)
Gd	LA-ICP-MS	LA-ICP-MS	59.7 (2.6)	130 (37)
Ho	LA-ICP-MS	LA-ICP-MS	65.3 (1.5)	107 (41)
Yb	LA-ICP-MS	LA-ICP-MS	71.4 (2.6)	110 (60)
Lu	LA-ICP-MS	LA-ICP-MS	71.9 (1.8)	113 (65)
Hf	SIMS	SIMS		
Ta	SIMS	SIMS		
W	LA-ICP-MS	LA-ICP-MS	54.4 (1.9)	580 (410)
Th	SIMS	SIMS		
U	SIMS	SIMS		

Note: Where 1σ <1, uncertainties in parentheses are expressed relative to last two significant figu

EPMA and mass balance data for silicate glass major elements from Hutchinson et al. (2020)

[a]Measurements of F by SIMS are subject to matrix effects. Since no matrix-matched standard was

		71 D3 1200 0.75		
D (SM - Sil)	**Sil (ppm)**	**SM (ppm)**	**D (SM - Sil)**	**Sil (ppm)**
2.56 (40)	54.2 (1.6)	121 (21)	**2.23 (39)**	53.2 (3.0)
2.46 (58)	25090 (590)	67000 (11000)	**2.69 (43)**	26100 (1700)
3.15 (64)	4400 (190)	15200 (3000)	**3.45 (71)**	4450 (140)
0.0136 (79)	78410 (770)	1500 (1600)	**0.019 (20)**	78210 (750)
0.0144 (65)	297100 (1300)	10500 (8700)	**0.035 (29)**	305300 (3500)
5.2 (4.3)	410 (110)	2000 (1700)	**4.9 (4.3)**	390 (110)
71.7 (5.9)	2809 (28)	222000 (18000)	**79.0 (6.6)**	2527 (64)
10.42 (73)	1166 (50)	14300 (1000)	**12.3 (1.0)**	1187 (28)
1.59 (36)	30620 (910)	47000 (15000)	**1.54 (48)**	34000 (1600)
9.86 (58)	20890 (310)	204000 (12000)	**9.78 (59)**	18830 (780)
0.63 (30)	91.5 (1.2)	47 (50)	**0.52 (54)**	78.0 (1.6)
0.226 (69)	2251 (58)	410 (150)	**0.182 (67)**	2599 (60)
1.7 (1.1)	81.5 (1.8)	112 (88)	**1.4 (1.1)**	74.4 (2.2)
3.1 (2.6)	570 (150)	2100 (1600)	**3.6 (2.9)**	250 (240)
0.57 (58)	16350 (410)	9600 (6600)	**0.58 (41)**	16320 (890)
2.9 (2.0)	79.2 (2.2)	140 (240)	**1.8 (3.1)**	143.7 (4.3)
1.6 (2.1)	62.2 (1.5)	43 (83)	**0.7 (1.3)**	65.5 (2.7)
16.0 (3.4)	93.3 (2.8)	1420 (470)	**15.2 (5.0)**	91.5 (2.0)
1.89 (72)	69.7 (2.2)	138 (51)	**1.98 (73)**	64.1 (1.8)
0.049 (27)	79.4 (2.8)	21.4 (4.0)	**0.270 (51)**	77.1 (2.1)
0.30 (13)	87.0 (1.5)	26 (29)	**0.30 (33)**	100.6 (2.3)
13 (12)	47.6 (2.7)	310 (560)	**7 (12)**	39.6 (2.1)
0.63 (62)	67.1 (1.6)	30 (110)	**0.4 (1.6)**	69.3 (3.9)
16 (12)	39.0 (2.2)	460 (500)	**12 (13)**	34.7 (1.2)
6.4 (2.2)	48.2 (1.1)	290 (110)	**6.1 (2.3)**	42.4 (1.1)
4.6 (1.5)	55.9 (1.8)	244 (85)	**4.4 (1.5)**	46.7 (1.4)
4.1 (1.2)	52.58 (64)	215 (58)	**4.1 (1.1)**	44.2 (1.5)
3.1 (1.1)	56.0 (1.4)	176 (58)	**3.1 (1.0)**	47.2 (2.3)
2.36 (82)	60.9 (2.5)	145 (50)	**2.38 (83)**	52.5 (2.6)
2.90 (97)	56.2 (1.5)	170 (57)	**3.0 (1.0)**	49.3 (1.5)
2.17 (63)	62.7 (1.2)	141 (42)	**2.24 (67)**	54.3 (2.9)
1.64 (63)	66.7 (2.4)	115 (35)	**1.73 (53)**	58.8 (1.4)
1.53 (84)	71.98 (96)	93 (52)	**1.30 (72)**	64.8 (1.7)
1.57 (91)	70.9 (2.0)	92 (60)	**1.30 (84)**	66.3 (2.0)
10.6 (7.6)	46.4 (4.1)	400 (4600)	**9 (99)**	50.5 (3.0)

.res, e.g. 0.0144 (65) indicates 0.0144 ± 0.0065

s available for anylses of sulfate melt, these numbers should be considered estimates.

87 **D2** **1200** **1**			**57** **D2** **1200** **0.75**	
SM (ppm)	**D (SM - Sil)**	**Sil (ppm)**	**SM (ppm)**	**D (SM - Sil)**
117 (23)	**2.19 (44)**	51.0 (1.6)	129 (17)	**2.52 (0.35)**
		334 (30)	1660 (210)	**4.97 (0.76)**
57000 (20000)	**2.19 (78)**	26100 (1100)	57000 (14000)	**2.18 (0.54)**
11800 (1800)	**2.66 (42)**	4140 (240)	13500 (2900)	**3.26 (0.72)**
		78860 (940)	940 (440)	**0.0119 (56)**
		302000 (1800)	3500 (2000)	**0.0116 (67)**
1800 (1300)	**4.5 (3.6)**	408 (59)	1660 (670)	**4.1 (1.8)**
222000 (16000)	**87.8 (6.8)**	2358 (51)	220000 (16000)	**93.3 (7.2)**
11410 (670)	**9.62 (61)**	958 (22)	12660 (670)	**13.21 (76)**
50000 (20000)	**1.46 (58)**	35040 (400)	43700 (7200)	**1.25 (21)**
179000 (13000)	**9.50 (79)**	17810 (570)	184000 (11000)	**10.33 (72)**
63 (35)	**0.81 (45)**	77.3 (1.5)	77 (50)	**0.99 (64)**
226 (99)	**0.087 (38)**	2619 (49)	670 (530)	**0.26 (20)**
110 (77)	**1.5 (1.0)**	74.8 (1.6)	115 (88)	**1.5 (1.2)**
		250 (200)	1090 (740)	**4.3 (4.6)**
12000 (10000)	**0.76 (0.63)**	16760 (590)	9900 (7000)	**0.59 (42)**
570 (270)	**4.0 (1.9)**	124.7 (4.4)	350 (240)	**2.8 (2.0)**
30 (21)	**0.46 (32)**	62.4 (2.2)	121 (83)	**1.9 (1.3)**
1610 (470)	**17.6 (5.2)**	82.5 (3.2)	1550 (470)	**18.8 (5.7)**
135 (46)	**2.11 (73)**	58.4 (2.4)	136 (51)	**2.33 (87)**
4.5 (4.1)	**0.058 (54)**	82.3 (1.9)	4.1 (4.0)	**0.049 (49)**
33 (18)	**0.33 (18)**	101.8 (1.9)	32 (29)	**0.32 (28)**
200 (180)	**5.1 (4.5)**	41.7 (1.6)	850 (560)	**20 (14)**
7.2 (5.0)	**0.104 (72)**	63.3 (2.3)	140 (110)	**2.1 (1.7)**
470 (260)	**13.5 (7.7)**	31.9 (1.1)	730 (500)	**23 (16)**
380 (120)	**9.0 (2.9)**	81 (17)	410 (110)	**5.1 (1.7)**
228 (71)	**4.9 (1.5)**	40.1 (1.7)	208 (85)	**5.2 (2.1)**
200 (59)	**4.5 (1.4)**	38.4 (2.1)	177 (58)	**4.6 (1.5)**
160 (52)	**3.4 (1.1)**	41.4 (2.7)	167 (58)	**4.0 (1.4)**
132 (42)	**2.52 (82)**	47.0 (2.7)	147 (50)	**3.1 (1.1)**
156 (54)	**3.2 (1.1)**	44.4 (1.8)	171 (57)	**3.9 (1.3)**
130 (40)	**2.39 (75)**	48.5 (4.4)	139 (42)	**2.87 (90)**
115 (42)	**1.95 (71)**	53.7 (2.0)	115 (35)	**2.14 (66)**
119 (50)	**1.84 (78)**	59.8 (2.3)	130 (52)	**2.17 (87)**
121 (53)	**1.83 (80)**	61.3 (2.8)	120 (60)	**1.96 (98)**
		68.8 (1.5)	1.20 (0.76)	**0.017 (11)**
		2.81 (54)	4.41 (0.26)	**1.57 (32)**
440 (380)	**8.8 (7.5)**	4000 (1700)	6300 (4600)	**1.6 (1.3)**
		81.2 (3.3)	20.1 (4.6)	**0.248 (57)**
		69.8 (2.4)	105 (28)	**1.51 (40)**

	69			**32**
	D2			**D2**
	1100			**1160**
	0.75			**0.2**
Sil (ppm)	**SM (ppm)**	**D (SM - Sil)**	**Sil (ppm)**	**SM (ppm)**
			57.6 (4.1)	110 (45)
474 (36)	4010 (710)	**8.5 (1.6)**		
			29400 (1500)	42000 (30000)
			5420 (150)	6800 (3000)
			78930 (790)	550 (290)
			297400 (3500)	3100 (3600)
			510 (110)	1400 (2100)
			2215 (83)	231000 (16000)
			1168 (20)	17200 (1100)
			34900 (1000)	50000 (21000)
			26200 (1100)	197000 (25000)
84.9 (1.6)	180 (11)	**2.12 (14)**	85.1 (2.2)	45 (36)
2663 (60)	590 (360)	**0.22 (13)**	2511 (96)	760 (260)
81.3 (1.9)	291 (60)	**3.58 (74)**	74.2 (2.9)	200 (230)
			360 (210)	550 (380)
			18270 (690)	
67.8 (1.1)	504 (61)	**7.43 (90)**	126.9 (3.9)	460 (500)
69.4 (1.6)	190 (120)	**2.7 (1.8)**	64.7 (2.0)	24 (24)
69.0 (1.7)	2040 (440)	**29.5 (6.4)**	128.7 (5.4)	1090 (230)
56.6 (1.5)	252 (57)	**4.5 (1.0)**	78.3 (4.6)	60 (10)
85.0 (2.1)	8.7 (2.2)	**0.102 (26)**	79.7 (3.2)	11.9 (9.6)
106.1 (2.6)	74.5 (7.3)	**0.702 (71)**	100.7 (2.1)	55 (53)
49.8 (2.9)	2310 (790)	**46 (16)**	38.7 (2.5)	350 (540)
70.1 (1.8)	206 (75)	**2.9 (1.1)**	67.9 (2.1)	10.8 (9.7)
40.8 (2.3)	1700 (340)	**41.6 (8.7)**	48.8 (1.7)	220 (170)
31.10 (92)	638 (91)	**20.5 (3.0)**	61.6 (3.1)	128 (20)
34.6 (1.3)	452 (19)	**13.08 (74)**	65.7 (2.8)	88 (17)
33.6 (1.2)	354 (85)	**10.6 (2.5)**	62.1 (2.2)	84 (13)
35.9 (1.3)	297 (61)	**8.3 (1.7)**	68.1 (2.6)	89 (20)
41.9 (1.6)	235 (37)	**5.59 (90)**	68.8 (4.5)	76 (19)
37.98 (0.92)	280 (61)	**7.4 (1.6)**	69.4 (3.1)	74 (16)
43.1 (1.8)	215 (55)	**5.0 (1.3)**	72.7 (4.1)	74 (21)
53.8 (1.7)	227 (41)	**4.22 (78)**	72.5 (1.1)	53 (12)
62.1 (1.8)	267 (33)	**4.30 (55)**	73.6 (1.2)	45 (14)
66.6 (1.6)	279 (61)	**4.19 (91)**	76.3 (3.4)	44 (12)
71.6 (3.5)	1.50 (0.59)	**0.0210 (83)**		
1.87 (59)	4.97 (73)	**2.66 (93)**		
60.2 (4.7)	2500 (1000)	**42 (17)**	45.9 (6.6)	420 (580)
85.1 (2.3)	19.2 (4.2)	**0.226 (50)**		
80.9 (1.5)	71 (20)	**0.88 (24)**		

		62 D1 1200 1		
D (SM - Sil)	**Sil (ppm)**	**SM (ppm)**	**D (SM - Sil)**	**Sil (ppm)**
1.91 (78)	63.7 (3.1)	211 (36)	**3.32 (59)**	47.7 (1.4)
				585 (19)
1.4 (1.0)	28230 (580)			29800 (1300)
1.26 (55)	5530 (120)			12660 (400)
0.0069 (36)	78320 (390)	310 (150)	**0.0039 (19)**	86130 (550)
0.011 (12)	302900 (1400)	2150 (730)	**0.0071 (24)**	254500 (2000)
2.7 (4.2)	350 (120)			1310 (140)
104.4 (8.3)	1966 (19)	226000 (18000)	**115.2 (9.0)**	5748 (56)
14.70 (95)	138 (26)			77 (14)
1.43 (59)	35030 (830)			24110 (420)
7.52 (99)	22570 (480)			39270 (430)
0.53 (42)	111.6 (6.0)	22.1 (7.8)	**0.198 (71)**	101.7 (1.9)
0.30 (10)	3105 (79)	261 (85)	**0.084 (27)**	5050 (120)
2.7 (3.2)	82.6 (6.7)	98 (50)	**1.19 (61)**	106.94 (0.88)
1.5 (1.4)	410 (240)	840 (410)	**2.0 (1.5)**	840 (390)
	17700 (490)			40530 (990)
3.6 (3.9)	149.2 (9.7)	146 (81)	**0.98 (54)**	147.6 (2.1)
0.37 (36)	91.0 (4.1)	63 (21)	**0.69 (23)**	87.0 (2.7)
8.5 (1.8)	150.4 (4.0)	1890 (690)	**12.6 (4.6)**	149.9 (2.8)
0.77 (14)	94.4 (6.2)	77 (22)	**0.82 (23)**	94.0 (3.5)
0.15 (12)	110.7 (5.5)	0.734 (0.065)	**0.00663 (67)**	100.9 (3.4)
0.55 (53)	121.1 (3.6)	20.3 (8.7)	**0.168 (72)**	107.4 (2.4)
9 (14)	49.4 (4.7)	610 (300)	**12.4 (6.2)**	60.2 (2.1)
0.16 (14)	102.7 (7.5)	63 (26)	**0.62 (26)**	120.7 (1.5)
4.5 (3.6)	57.5 (3.6)	490 (150)	**8.5 (2.6)**	59.4 (2.3)
2.08 (34)	72.4 (6.0)	263 (71)	**3.6 (1.0)**	73.3 (2.1)
1.34 (27)	79.8 (5.2)	178 (51)	**2.23 (66)**	119.8 (3.9)
1.35 (21)	79.4 (4.7)	166 (44)	**2.09 (57)**	81.1 (3.1)
1.31 (30)	86.1 (4.5)	142 (40)	**1.65 (47)**	86.0 (2.8)
1.11 (29)	90.0 (5.7)	114 (32)	**1.27 (36)**	90.4 (2.1)
1.07 (23)	79.9 (4.7)	146 (42)	**1.83 (54)**	83.7 (3.3)
1.02 (29)	89.6 (6.9)	102 (31)	**1.13 (36)**	87.6 (3.8)
0.73 (17)	90.6 (5.5)	76 (18)	**0.84 (21)**	84.8 (2.8)
0.61 (18)	94.7 (6.8)	56 (15)	**0.60 (16)**	91.8 (3.1)
0.58 (16)	98.1 (8.2)	57 (15)	**0.58 (16)**	95.4 (1.8)
9 (13)	83 (29)	640 (200)	**7.7 (3.6)**	67.2 (2.2)

23			**22**	
A1			**A1**	
1200			**1100**	
1			**1**	
SM (ppm)	**D (SM - Sil)**	**Sil (ppm)**	**SM (ppm)**	**D (SM - Sil)**
131 (15)	**2.75 (32)**			
1800 (1200)	**3.1 (2.1)**	754 (21)	7800 (3600)	**10.4 (4.8)**
56000 (16000)	**1.87 (55)**			
17300 (5300)	**1.37 (42)**			
1020 (560)	**0.0118 (65)**			
3600 (1900)	**0.0143 (76)**			
5600 (1700)	**4.3 (1.4)**			
226000 (17000)	**39.3 (3.0)**			
460 (170)	**6.0 (2.4)**			
37000 (6600)	**1.53 (28)**			
178000 (13000)	**4.54 (33)**			
22 (12)	**0.22 (11)**	92.9 (6.0)	88 (47)	**0.95 (51)**
720 (230)	**0.143 (46)**	5020 (270)	2038 (84)	**0.406 (27)**
101 (59)	**0.94 (55)**	123 (11)	480 (250)	**3.9 (2.0)**
1760 (590)	**2.1 (1.2)**			
10000 (13000)	**0.25 (33)**			
116 (78)	**0.79 (53)**	159 (18)	530 (310)	**3.3 (2.0)**
28 (17)	**0.32 (19)**	99.4 (5.7)	250 (250)	**2.5 (2.5)**
1420 (470)	**9.4 (3.1)**	120.0 (9.8)	1900 (1100)	**15.7 (9.1)**
66 (18)	**0.70 (19)**	86.3 (5.9)	107 (13)	**1.24 (17)**
8.1 (4.3)	**0.080 (42)**	94.6 (7.1)	18.2 (9.6)	**0.19 (10)**
18.6 (9.4)	**0.173 (87)**	111.8 (9.3)	76 (25)	**0.68 (23)**
42 (44)	**0.69 (72)**	80.7 (7.2)	1900 (1600)	**24 (20)**
15.7 (9.3)	**0.130 (77)**	133.9 (8.0)	110 (110)	**0.80 (80)**
390 (290)	**6.6 (4.8)**	74.6 (5.5)	1200 (1300)	**17 (17)**
148 (50)	**2.02 (68)**	68.6 (5.3)	269 (22)	**3.93 (44)**
197 (48)	**1.64 (40)**	119 (11)	298 (36)	**2.50 (38)**
108 (30)	**1.33 (37)**	75.0 (3.8)	172 (13)	**2.29 (21)**
93 (24)	**1.08 (28)**	75.1 (5.7)	158 (32)	**2.10 (45)**
81 (23)	**0.90 (25)**	76.1 (6.8)	119 (29)	**1.56 (40)**
99 (29)	**1.19 (36)**	75.0 (9.3)	131 (24)	**1.75 (38)**
81 (19)	**0.92 (22)**	80.9 (8.7)	111 (32)	**1.37 (43)**
59 (17)	**0.70 (20)**	79.9 (5.6)	97 (17)	**1.21 (23)**
43 (15)	**0.47 (16)**	86.7 (4.4)	80 (20)	**0.92 (23)**
42 (13)	**0.44 (14)**	86.1 (5.7)	87 (25)	**1.01 (30)**
		90.4 (4.9)	1.00 (66)	**0.0111 (74)**
		5.74 (79)	2.80 (67)	**0.49 (13)**
100 (160)	**1.5 (2.4)**	89 (10)	2700 (1600)	**30 (19)**
		107.0 (5.8)	8.4 (2.2)	**0.079 (21)**
		93.1 (5.2)	26.41 (84)	**0.284 (18)**

This is the peer-reviewed, final accepted version for American Mineralogist, published by the Mineralogical Society of America.
The published version is subject to change. Cite as Authors (Year) Title. American Mineralogist, in press.
DOI: https://doi.org/10.2138/am-2022-8345. http://www.minsocam.org/

	Run #			61	
	Starting Composition			D2	
	Temperature (°C)			1000	
	Pressure (GPa)			1	
	Sil Method	Anh Method	Sil (ppm)	Anh (ppm)	D (Anh - Sil)
F	SIMS	SIMS	414 (32)	4.4 (2.4)	**0.0106 (58)**
Cl	EPMA	SIMS	2424 (33)	108 (19)	**0.0444 (77)**
Li	SIMS	SIMS	97.4 (2.1)	0.822 (33)	**0.00844 (39)**
Na	EPMA	SIMS	33250 (940)	312.6 (7.5)	**0.00940 (35)**
K	EPMA	SIMS	39850 (640)	68.3 (9.4)	**0.00171 (24)**
Rb	SIMS	SIMS	58.4 (1.8)	0.057 (27)	**0.00097 (47)**
Mg	EPMA	SIMS	6190 (130)	317 (24)	**0.0512 (40)**
Mn	SIMS	SIMS	213.3 (9.0)	34.8 (1.2)	**0.1632 (89)**
Ca	EPMA	Stoichiometry	6080 (450)	294500 (2900)	**48.4 (3.7)**
Sr	SIMS	SIMS	60.6 (4.9)	1190 (180)	**19.7 (3.3)**
Ba	SIMS	SIMS	62.2 (2.7)	39.6 (5.9)	**0.637 (99)**
La	SIMS	SIMS	22.6 (1.7)	209 (12)	**9.23 (87)**
Ce	SIMS	SIMS	25.2 (1.7)	180 (11)	**7.15 (64)**
Pr	SIMS	SIMS	21.6 (1.6)	173.5 (6.7)	**8.03 (65)**
Nd	SIMS	SIMS	23.9 (2.2)	218.1 (6.7)	**9.12 (89)**
Sm	SIMS	SIMS	24.3 (1.6)	245 (10)	**10.08 (79)**
Eu	SIMS	SIMS	25.3 (1.4)	304 (10)	**12.02 (79)**
Gd	SIMS	SIMS	27.5 (2.7)	219.6 (3.1)	**7.99 (80)**
Yb	SIMS	SIMS	44.3 (3.4)	56.8 (3.1)	**1.28 (12)**
Ho	SIMS	SIMS	37.5 (2.0)	108.4 (2.6)	**2.89 (17)**
Y	SIMS	SIMS	42.0 (1.6)	101.5 (2.5)	**2.42 (11)**
Lu	SIMS	SIMS	48.0 (1.8)	41.2 (1.9)	**0.859 (51)**
Sc	SIMS	SIMS	70.7 (1.3)	3.39 (98)	**0.048 (14)**
Si	EPMA	SIMS	298400 (1500)	15 (11)	**0.000049 (37)**
P	EPMA	SIMS	601 (82)	128 (15)	**0.213 (38)**
S	EPMA	Stoichiometry	1412 (56)	235500 (2400)	**166.7 (6.8)**
Ti	EPMA	SIMS	2220 (160)	1.35 (33)	**0.00061 (15)**
V	SIMS	SIMS	81.0 (1.5)	0.488 (46)	**0.00603 (58)**
Nb	SIMS	SIMS	86.7 (2.3)		
Mo	SIMS	SIMS	79.1 (5.9)	10.14 (33)	**0.128 (10)**
Zr	SIMS	SIMS	64.2 (2.0)	0.041 (19)	**0.00063 (29)**
Hf	SIMS	SIMS	63.7 (3.8)	0.019 (75)	**0.0003 (12)**
Ta	SIMS	SIMS	1.61 (78)	4.18 (85)	**2.6 (1.4)**
W	SIMS	SIMS	78.6 (7.6)	3.0 (1.4)	**0.038 (18)**
Pb	SIMS	SIMS	5.8 (1.6)	3.10 (90)	**0.53 (21)**
Th	SIMS	SIMS	79.4 (3.1)	0.28 (10)	**0.0035 (13)**
U	SIMS	SIMS	76.1 (3.0)	0.017 (29)	**0.00022 (39)**

Note: Where 1σ <1, uncertainties in parentheses are expressed relative to last two significant figures, e.g. 0.0144 (
EPMA data for silicate glass major elements from Hutchinson et al. (2020)

	69			**16**
	D2			**D2**
	1100			**1050**
	0.75			**0.75**
Sil (ppm)	**Anh (ppm)**	**D (Anh - Sil)**	**Sil (ppm)**	**Anh (ppm)**
474 (36)	2.4 (2.7)	**0.0051 (58)**	395.7 (7.9)	2.1 (1.8)
1483 (45)	90 (37)	**0.061 (25)**	1990 (110)	62 (21)
80.3 (1.5)	1.01 (22)	**0.0125 (27)**	88.1 (1.2)	0.56 (38)
28780 (710)	378 (84)	**0.0131 (30)**	30720 (840)	324 (25)
37210 (570)	96 (65)	**0.0026 (17)**	38630 (540)	51.3 (6.8)
60.6 (1.5)	0.131 (89)	**0.0022 (15)**	59.6 (2.1)	0.096 (72)
4760 (260)	294 (21)	**0.0617 (55)**	5420 (240)	269.3 (5.6)
269.9 (7.3)	37.1 (2.7)	**0.137 (11)**	286 (14)	44.5 (5.3)
9910 (360)	294500 (2900)	**29.7 (1.1)**	9140 (290)	294500 (2900)
71.8 (5.1)	1190 (51)	**16.6 (1.4)**	70.11 (89)	1230 (110)
41.18 (81)	32.98 (89)	**0.801 (27)**	49.4 (2.9)	31 (10)
24.6 (1.5)	222 (17)	**9.02 (88)**	26.62 (83)	215 (15)
28.0 (1.6)	199 (20)	**7.09 (82)**	29.85 (21)	190 (11)
26.9 (1.8)	199 (18)	**7.39 (82)**	27.73 (63)	187 (10)
27.6 (2.3)	256 (24)	**9.3 (1.2)**	28.8 (1.3)	239.2 (8.2)
28.1 (1.5)	289 (26)	**10.3 (1.1)**	30.03 (88)	267 (14)
30.4 (1.8)	365 (13)	**12.00 (84)**	30.58 (53)	340 (26)
35.0 (4.2)	261 (19)	**7.4 (1.0)**	37.8 (1.8)	246 (13)
48.2 (1.0)	71.8 (5.2)	**1.49 (11)**	50.0 (1.9)	60.7 (5.9)
43.0 (1.9)	138.3 (8.4)	**3.22 (24)**	43.0 (1.4)	125.1 (6.5)
44.1 (1.3)	130 (13)	**2.95 (30)**	45.12 (51)	115.1 (4.9)
53.16 (83)	55.6 (3.6)	**1.046 (69)**	53.5 (2.1)	47.0 (3.7)
72.8 (1.0)	1.796 (53)	**0.02468 (81)**	73.5 (1.5)	1.113 (88)
303400 (1500)	4.1 (1.4)	**0.0000135 (45)**	302800 (1700)	3.0 (1.0)
530 (130)	106 (24)	**0.200 (66)**	570 (88)	169 (31)
1740 (100)	235500 (2400)	**135.5 (8.0)**	1463 (20)	235500 (2400)
2480 (160)	1.27 (16)	**0.000511 (71)**	2519 (90)	1.69 (47)
86.8 (1.2)	0.353 (59)	**0.00406 (68)**	86.2 (1.9)	0.37 (11)
94.3 (2.4)			87.5 (2.2)	12.1 (4.0)
55.2 (5.0)	5.3 (4.3)	**0.096 (78)**	67.0 (9.5)	0.48 (29)
68.5 (1.0)	0.088 (77)	**0.0013 (11)**	67.0 (1.8)	0.078 (70)
71.6 (3.5)	0.14 (17)	**0.0019 (23)**	70.8 (5.7)	0.03 (11)
1.87 (59)	4.3 (1.0)	**2.32 (92)**	1.72 (26)	5.11 (22)
65.3 (7.7)	4.2 (1.7)	**0.064 (26)**	81.7 (9.7)	2.6 (1.2)
13.3 (1.3)	5.16 (78)	**0.387 (70)**	5.3 (1.2)	2.23 (67)
85.1 (2.3)	0.56 (23)	**0.0065 (27)**	82.5 (3.8)	0.39 (18)
80.9 (1.5)	0.025 (21)	**0.00031 (27)**	80.8 (5.2)	0.08 (13)

(65) indicates 0.0144 ± 0.0065

This is the peer-reviewed, final accepted version for American Mineralogist, published by the Mineralogical Society of America.
The published version is subject to change. Cite as Authors (Year) Title. American Mineralogist, in press.
DOI: https://doi.org/10.2138/am-2022-8345. http://www.minsocam.org/

		24 D2 1000 0.75		
D (Anh - Sil)	**Sil (ppm)**	**Anh (ppm)**	**D (Anh - Sil)**	**Sil (ppm)**
0.0052 (45)	438 (48)	1.23 (47)	**0.0028 (11)**	384 (47)
0.031 (11)	2169 (22)	25.4 (3.2)	**0.0117 (15)**	2382 (28)
0.0063 (43)	96.1 (1.2)	0.769 (34)	**0.00800 (37)**	111.0 (5.9)
0.01056 (86)	32400 (1100)	315 (17)	**0.00972 (61)**	33790 (870)
0.00133 (18)	39520 (680)	36.8 (1.4)	**0.000931 (39)**	40360 (670)
0.0016 (12)	59.7 (2.1)	0.09 (12)	**0.0015 (20)**	61.7 (2.3)
0.0497 (24)	5590 (190)	275.1 (7.1)	**0.0493 (21)**	3240 (170)
0.155 (20)	214.6 (3.6)	41.98 (30)	**0.1956 (36)**	179 (19)
32.2 (1.1)	6570 (310)	294500 (2900)	**44.8 (2.1)**	2510 (150)
17.6 (1.6)	53.7 (2.5)	1166 (51)	**21.7 (1.4)**	39 (12)
0.63 (21)	54.4 (2.2)	33.420 (97)	**0.614 (24)**	54.5 (1.1)
8.09 (63)	21.5 (1.4)	207 (14)	**9.66 (92)**	11.7 (1.1)
6.36 (37)	24.35 (48)	186 (13)	**7.62 (56)**	13.4 (1.1)
6.76 (40)	21.90 (61)	184 (14)	**8.41 (69)**	11.7 (1.0)
8.32 (48)	21.5 (2.4)	233 (15)	**10.8 (1.4)**	12.5 (1.1)
8.89 (53)	23.4 (1.2)	256 (26)	**11.0 (1.3)**	12.59 (72)
11.11 (86)	23.5 (1.1)	342 (21)	**14.5 (1.1)**	13.14 (74)
6.51 (45)	27.3 (2.1)	232 (28)	**8.5 (1.2)**	15.7 (1.3)
1.21 (13)	45.9 (6.0)	75.3 (2.6)	**1.64 (22)**	33.4 (2.4)
2.91 (18)	37.0 (1.6)	125.8 (9.0)	**3.40 (29)**	22.9 (1.8)
2.55 (11)	39.9 (1.0)	115.2 (8.0)	**2.89 (21)**	25.9 (1.7)
0.878 (77)	49.0 (1.1)	54.5 (1.9)	**1.111 (46)**	37.9 (1.3)
0.0151 (12)	71.13 (55)	0.688 (58)	**0.00967 (81)**	58.5 (1.6)
0.0000098 (33)	302400 (1700)	5.70 (52)	**0.0000189 (17)**	308600 (1900)
0.296 (71)	628 (73)	174 (11)	**0.277 (36)**	600 (130)
161.0 (2.8)	1317 (21)	235500 (2400)	**178.8 (3.3)**	1072 (85)
0.00067 (19)	2370 (100)	1.73 (12)	**0.000729 (59)**	1087 (85)
0.0043 (12)	82.5 (1.5)	0.295 (20)	**0.00358 (25)**	49.56 (72)
0.138 (45)	88.9 (1.6)	5.7 (4.9)	**0.064 (55)**	80.8 (1.8)
0.0072 (44)	64.9 (2.9)	3.3 (4.5)	**0.051 (69)**	77.5 (8.3)
0.0012 (10)	65.4 (1.9)	0.0228 (43)	**0.000348 (67)**	66.2 (1.4)
0.0004 (16)	67.8 (5.0)	0.21 (17)	**0.0031 (25)**	67.23 (81)
2.97 (46)	1.83 (66)	5.3 (1.5)	**2.9 (1.3)**	0.6 (1.7)
0.032 (15)	77.8 (7.5)	2.77 (68)	**0.0357 (94)**	80 (11)
0.42 (16)	3.9 (1.8)	2.72 (28)	**0.70 (33)**	10.4 (2.3)
0.0047 (22)	81.8 (2.1)	0.598 (67)	**0.00731 (84)**	81.2 (1.3)
0.0010 (16)	80.8 (1.7)	0.058 (11)	**0.00071 (14)**	80.4 (1.9)

This is the peer-reviewed, final accepted version for American Mineralogist, published by the Mineralogical Society of America.
The published version is subject to change. Cite as Authors (Year) Title. American Mineralogist, in press.
DOI: https://doi.org/10.2138/am-2022-8345. http://www.minsocam.org/

68			**54**	
D2			**D2**	
900			**1000**	
0.75			**0.2**	
Anh (ppm)	**D (Anh - Sil)**	**Sil (ppm)**	**Anh (ppm)**	**D (Anh - Sil)**
1.34 (88)	**0.0035 (23)**	503 (34)	0.8 (1.5)	**0.0015 (30)**
300 (390)	**0.13 (16)**	1757 (41)	61 (70)	**0.034 (40)**
0.72 (15)	**0.0065 (14)**	94.2 (2.8)	0.54 (18)	**0.0057 (19)**
324 (38)	**0.0096 (11)**	32090 (710)	308 (30)	**0.00959 (97)**
82 (14)	**0.00203 (36)**	41180 (330)	63 (15)	**0.00153 (37)**
0.050 (36)	**0.00082 (58)**	64.2 (2.4)	0.024 (76)	**0.0004 (12)**
328 (12)	**0.1012 (65)**	4820 (280)	216 (12)	**0.0449 (36)**
37.8 (3.9)	**0.211 (32)**	173.3 (4.4)	27.9 (2.7)	**0.161 (16)**
294500 (2900)	**117.5 (7.1)**	5650 (270)	294500 (2900)	**52.2 (2.5)**
1067 (78)	**27.1 (8.2)**	62.2 (7.2)	1247 (89)	**20.1 (2.7)**
37.0 (1.1)	**0.679 (24)**	53.9 (2.1)	32.1 (4.1)	**0.596 (79)**
207 (15)	**17.7 (2.0)**	19.9 (1.1)	204 (15)	**10.27 (92)**
177 (18)	**13.2 (1.7)**	22.5 (1.4)	168 (14)	**7.45 (78)**
179 (15)	**15.3 (1.9)**	21.15 (92)	173 (13)	**8.17 (69)**
232 (22)	**18.5 (2.4)**	21.9 (1.0)	232 (14)	**10.60 (81)**
256 (20)	**20.3 (2.0)**	23.0 (1.5)	251 (20)	**10.9 (1.1)**
307 (21)	**23.3 (2.1)**	25.83 (94)	335 (20)	**12.98 (90)**
240 (13)	**15.3 (1.5)**	28.55 (98)	231 (17)	**8.10 (65)**
71.1 (8.0)	**2.13 (29)**	44.8 (2.6)	58.2 (4.8)	**1.30 (13)**
128 (11)	**5.58 (64)**	35.9 (2.0)	115.2 (7.5)	**3.21 (28)**
119.4 (8.6)	**4.60 (45)**	38.9 (1.1)	105.0 (7.1)	**2.70 (20)**
54.6 (5.9)	**1.44 (16)**	48.9 (1.3)	42.9 (3.2)	**0.877 (70)**
1.18 (18)	**0.0201 (31)**	64.4 (2.9)	1.00 (21)	**0.0155 (34)**
3.8 (1.3)	**0.0000124 (42)**	307000 (2300)	2.8 (2.4)	**0.0000090 (77)**
135 (26)	**0.223 (66)**	563 (73)	121 (21)	**0.214 (47)**
235500 (2400)	**220 (18)**	1008 (58)	235500 (2400)	**234 (14)**
1.45 (24)	**0.00134 (24)**	1890 (210)	0.95 (27)	**0.00050 (15)**
0.389 (53)	**0.0078 (11)**	86.0 (2.4)	0.533 (0.058)	**0.00619 (70)**
9.1 (1.3)	**0.112 (17)**	93.0 (4.4)	0.1 (2.7)	**0.002 (29)**
0.277 (87)	**0.0036 (12)**	57.0 (4.5)	1.1 (2.0)	**0.020 (36)**
0.017 (38)	**0.00025 (57)**	65.7 (2.0)	0.053 (40)	**0.00081 (61)**
0.097 (96)	**0.0014 (14)**	68.1 (2.8)	0.25 (13)	**0.0037 (19)**
4.26 (55)	**7 (19)**	2.21 (68)	4.93 (84)	**2.23 (78)**
2.37 (42)	**0.0296 (67)**	64.0 (3.2)	4.7 (1.0)	**0.074 (17)**
7.30 (82)	**0.70 (17)**	7.60 (78)	2.45 (63)	**0.323 (89)**
0.395 (91)	**0.0049 (11)**	85.4 (3.3)	0.22 (13)	**0.0026 (15)**
0.13 (19)	**0.0016 (24)**	78.4 (2.7)		

	22 A1 1100 1	
Sil (ppm)	**Anh (ppm)**	**D (Anh - Sil)**
754 (21)	2.2 (1.5)	**0.0029 (20)**
79 (11)	21 (70)	**0.27 (89)**
60.94 (23)	0.92 (18)	**0.0150 (29)**
34400 (1200)	133 (30)	**0.00387 (89)**
28700 (1200)	21 (15)	**0.00074 (52)**
80.10 (21)	0.079 (76)	**0.00098 (95)**
14100 (260)	198 (12)	**0.01401 (86)**
641.4 (5.0)	30.5 (2.7)	**0.0475 (43)**
30160 (780)	294500 (2900)	**9.76 (27)**
121.1 (2.0)	934 (89)	**7.71 (75)**
78.4 (6.9)	37.7 (4.1)	**0.480 (67)**
67.4 (4.1)	122 (15)	**1.80 (24)**
114.2 (5.3)	159 (14)	**1.39 (14)**
69.9 (4.4)	102 (13)	**1.46 (20)**
71.3 (5.2)	122 (14)	**1.71 (23)**
70.4 (3.9)	124 (20)	**1.76 (29)**
72.0 (3.4)	169 (20)	**2.35 (30)**
81.8 (6.1)	111 (17)	**1.36 (23)**
79.1 (6.3)	22.6 (4.8)	**0.286 (64)**
79.9 (3.1)	48.1 (7.5)	**0.602 (97)**
84.2 (3.8)	47.1 (7.1)	**0.560 (88)**
80.8 (4.1)	15.4 (3.2)	**0.190 (41)**
94.36 (28)	0.27 (21)	**0.0028 (23)**
255300 (2400)	4.4 (2.4)	**0.0000171 (93)**
1560 (120)	200 (21)	**0.128 (17)**
4598 (66)	235500 (2400)	**51.21 (90)**
5320 (140)	3.13 (27)	**0.000588 (53)**
114.5 (1.2)	0.569 (58)	**0.00497 (51)**
99.4 (1.1)		
73.2 (5.6)	1.3 (2.0)	**0.018 (28)**
95.2 (3.7)	0.062 (40)	**0.00066 (42)**
90.4 (4.9)	0.11 (13)	**0.0012 (14)**
5.74 (79)	1.70 (84)	**0.30 (15)**
77.0 (6.1)	4.7 (1.0)	**0.061 (14)**
7.8 (1.9)	1.56 (63)	**0.199 (94)**
107.0 (5.8)	0.19 (13)	**0.0018 (12)**
93.1 (5.2)	0.482 (74)	**0.00517 (84)**

Figure 1

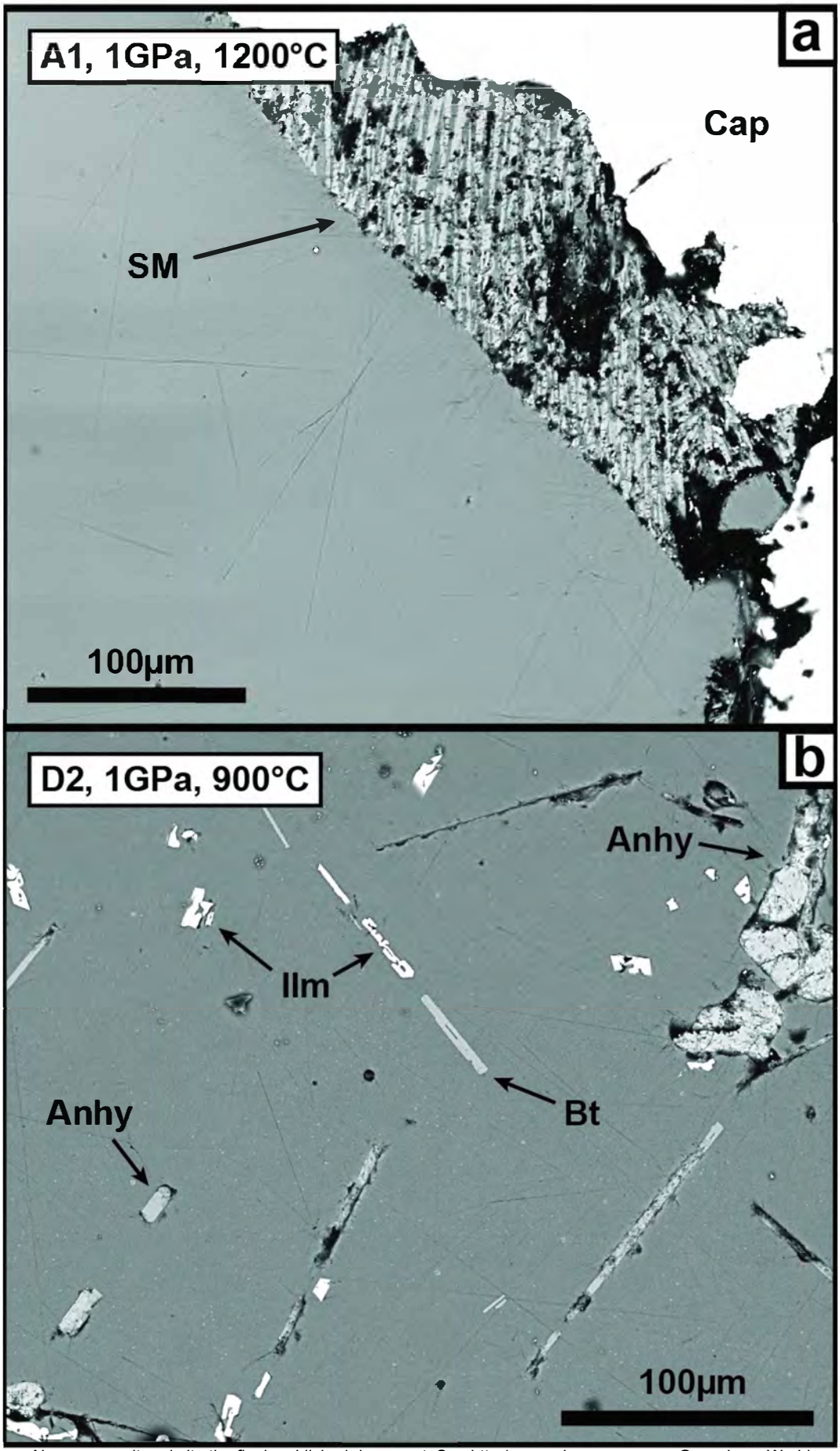

This is the peer-reviewed, final accepted version for American Mineralogist, published by the Mineralogical Society of America.
The published version is subject to change. Cite as Authors (Year) Title. American Mineralogist, in press.
DOI: https://doi.org/10.2138/am-2022-8345. http://www.minsocam.org/

Figure 2

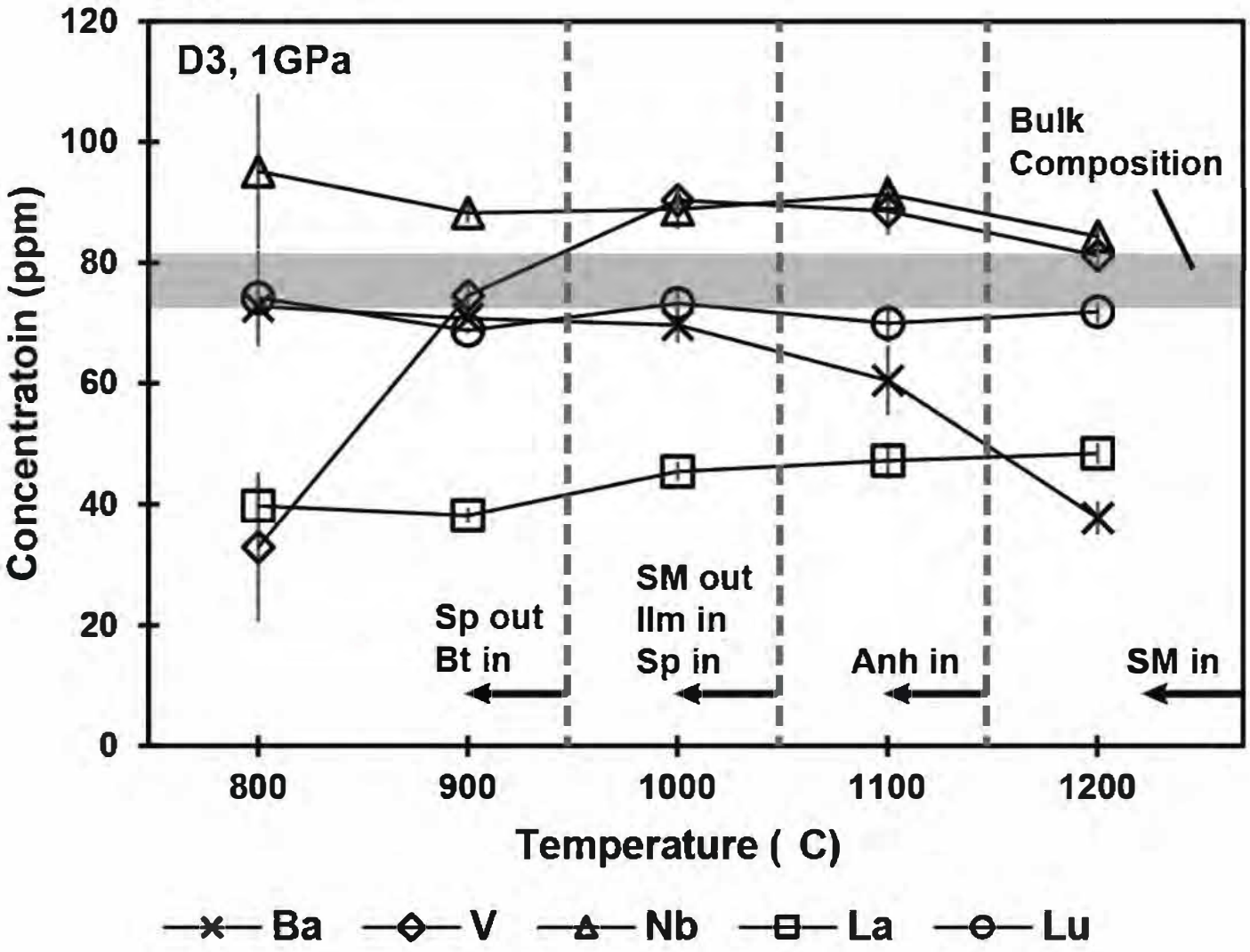

This is the peer-reviewed, final accepted version for American Mineralogist, published by the Mineralogical Society of America.
The published version is subject to change. Cite as Authors (Year) Title. American Mineralogist, in press.
DOI: https://doi.org/10.2138/am-2022-8345. http://www.minsocam.org/

Figure 3

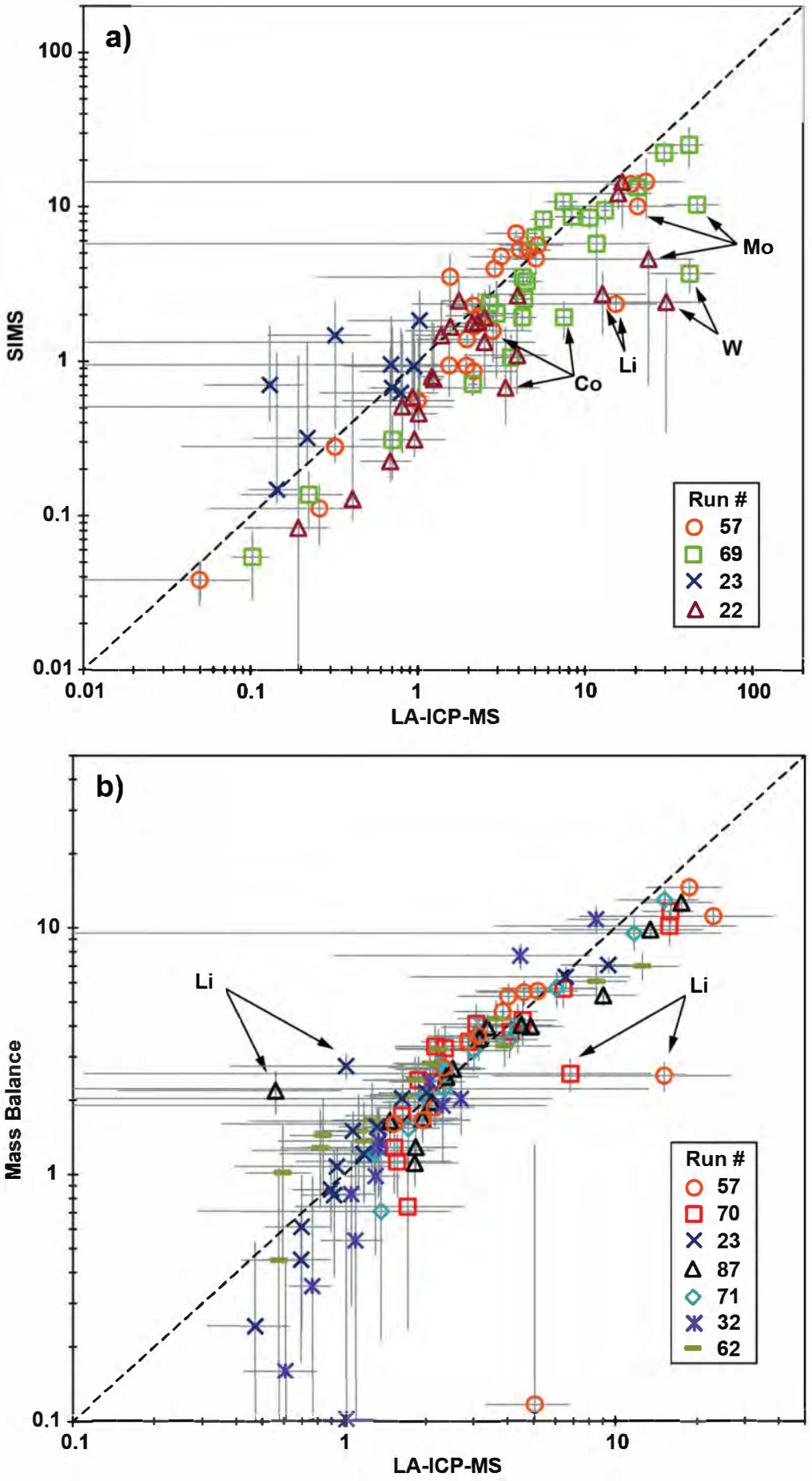

This is the peer-reviewed, final accepted version for American Mineralogist, published by the Mineralogical Society of America.
The published version is subject to change. Cite as Authors (Year) Title. American Mineralogist, in press.
DOI: https://doi.org/10.2138/am-2022-8345. http://www.minsocam.org/

Figure 4

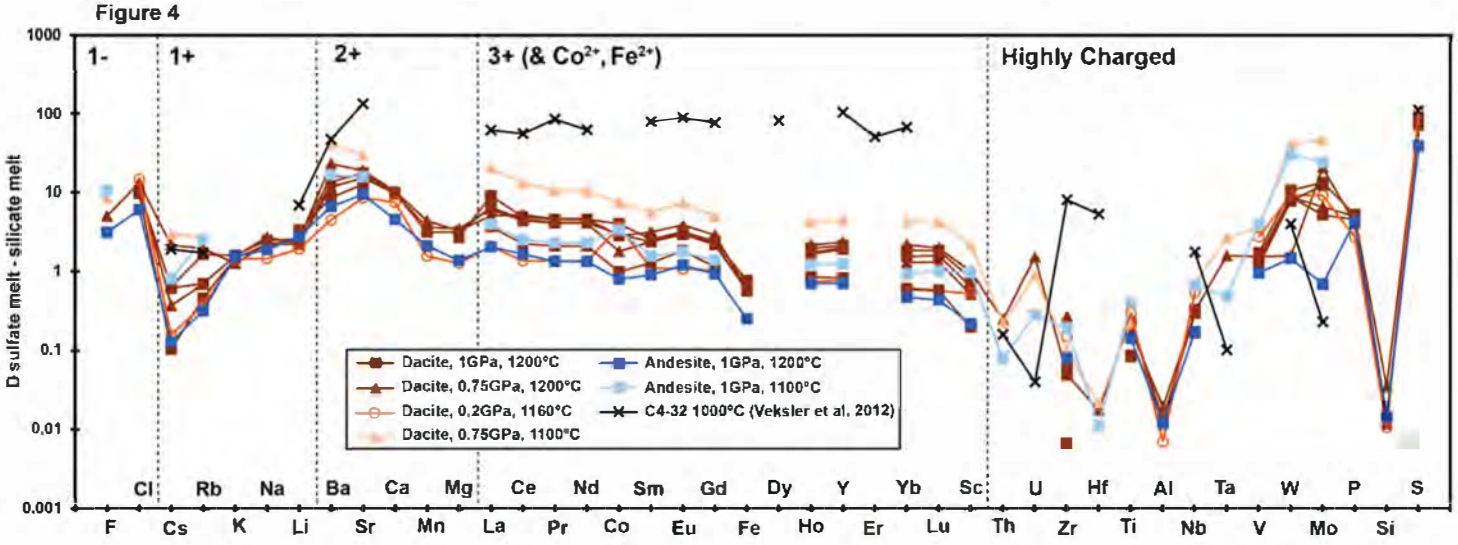

This is the peer-reviewed, final accepted version for American Mineralogist, published by the Mineralogical Society of America.
The published version is subject to change. Cite as Authors (Year) Title. American Mineralogist, in press.
DOI: https://doi.org/10.2138/am-2022-8345. http://www.minsocam.org/

Figure 5

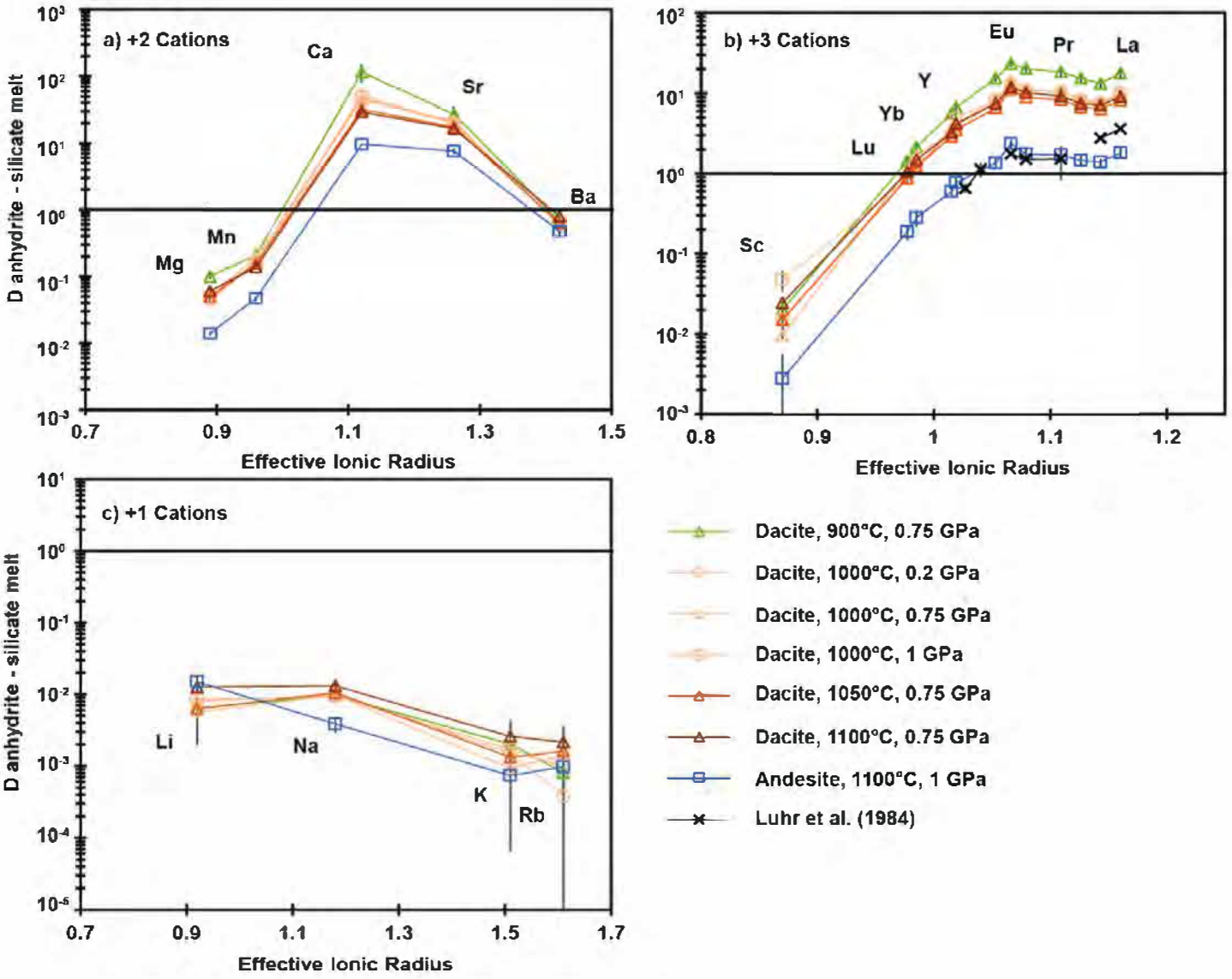

This is the peer-reviewed, final accepted version for American Mineralogist, published by the Mineralogical Society of America.
The published version is subject to change. Cite as Authors (Year) Title. American Mineralogist, in press.
DOI: https://doi.org/10.2138/am-2022-8345. http://www.minsocam.org/

Figure 6

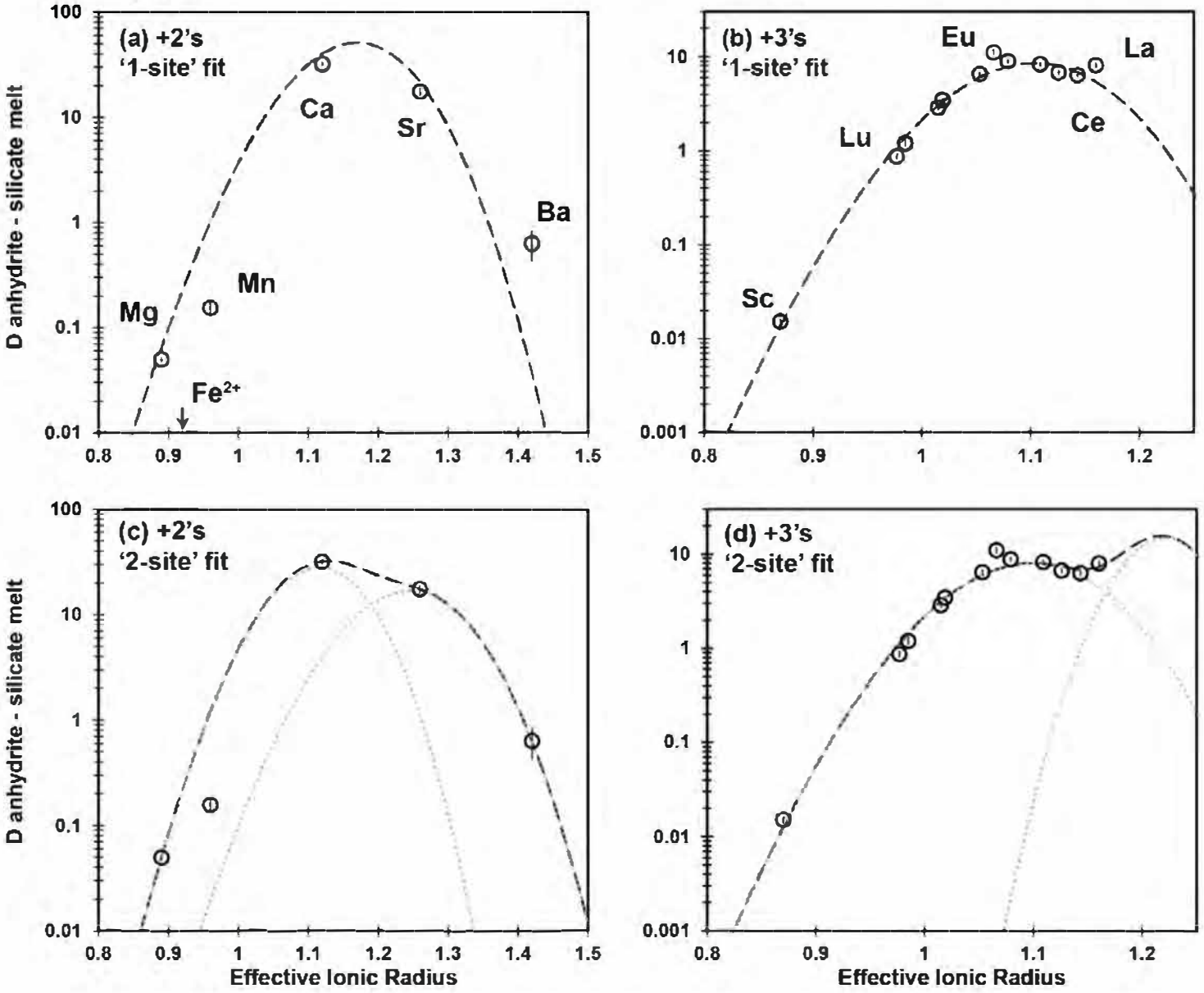

Figure 7

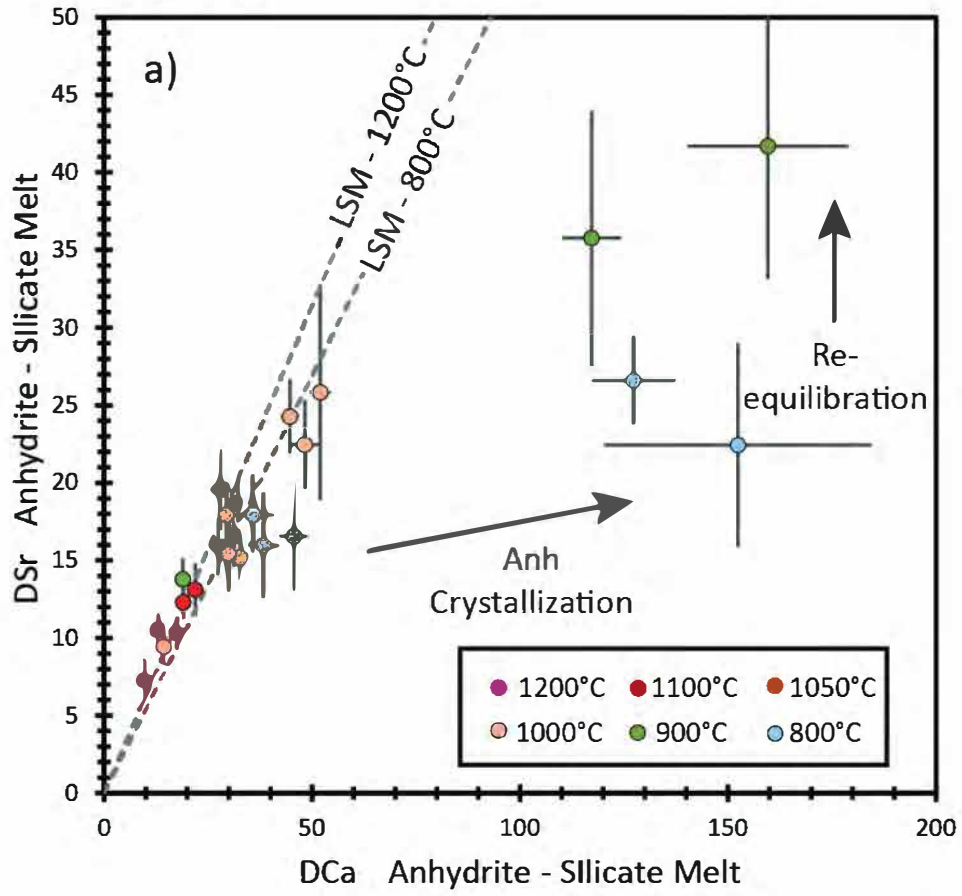

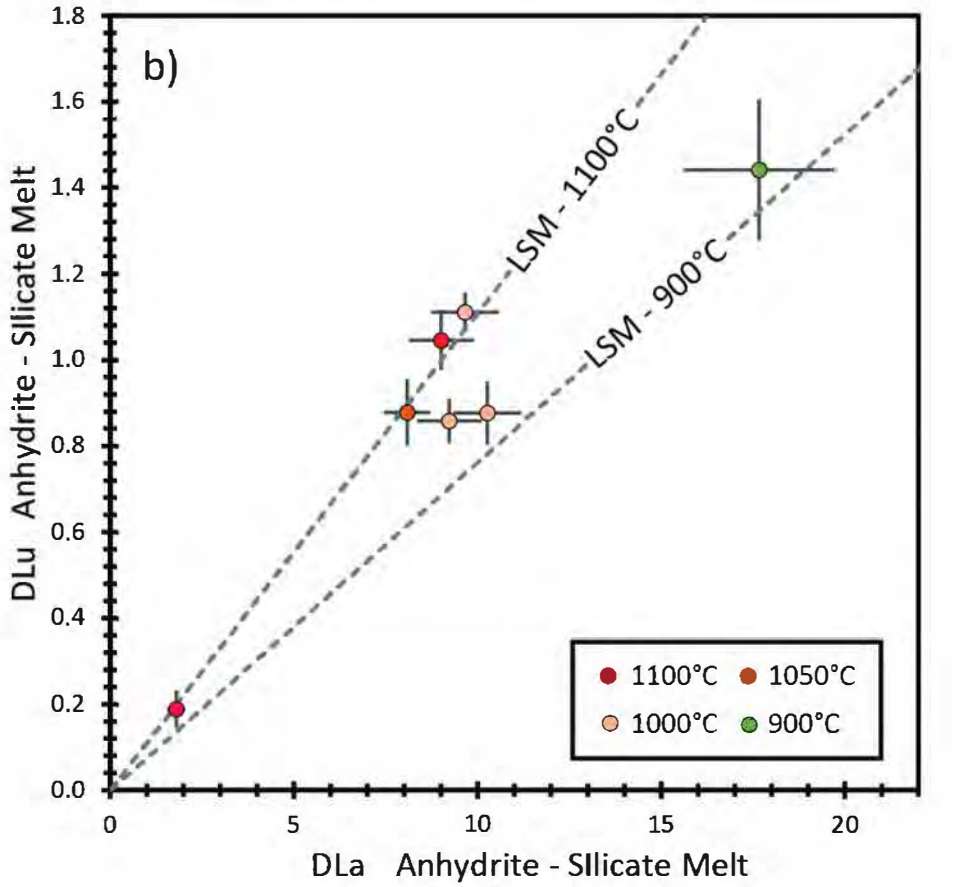

This is the peer-reviewed, final accepted version for American Mineralogist, published by the Mineralogical Society of America.
The published version is subject to change. Cite as Authors (Year) Title. American Mineralogist, in press.
DOI: https://doi.org/10.2138/am-2022-8345. http://www.minsocam.org/

Figure 8

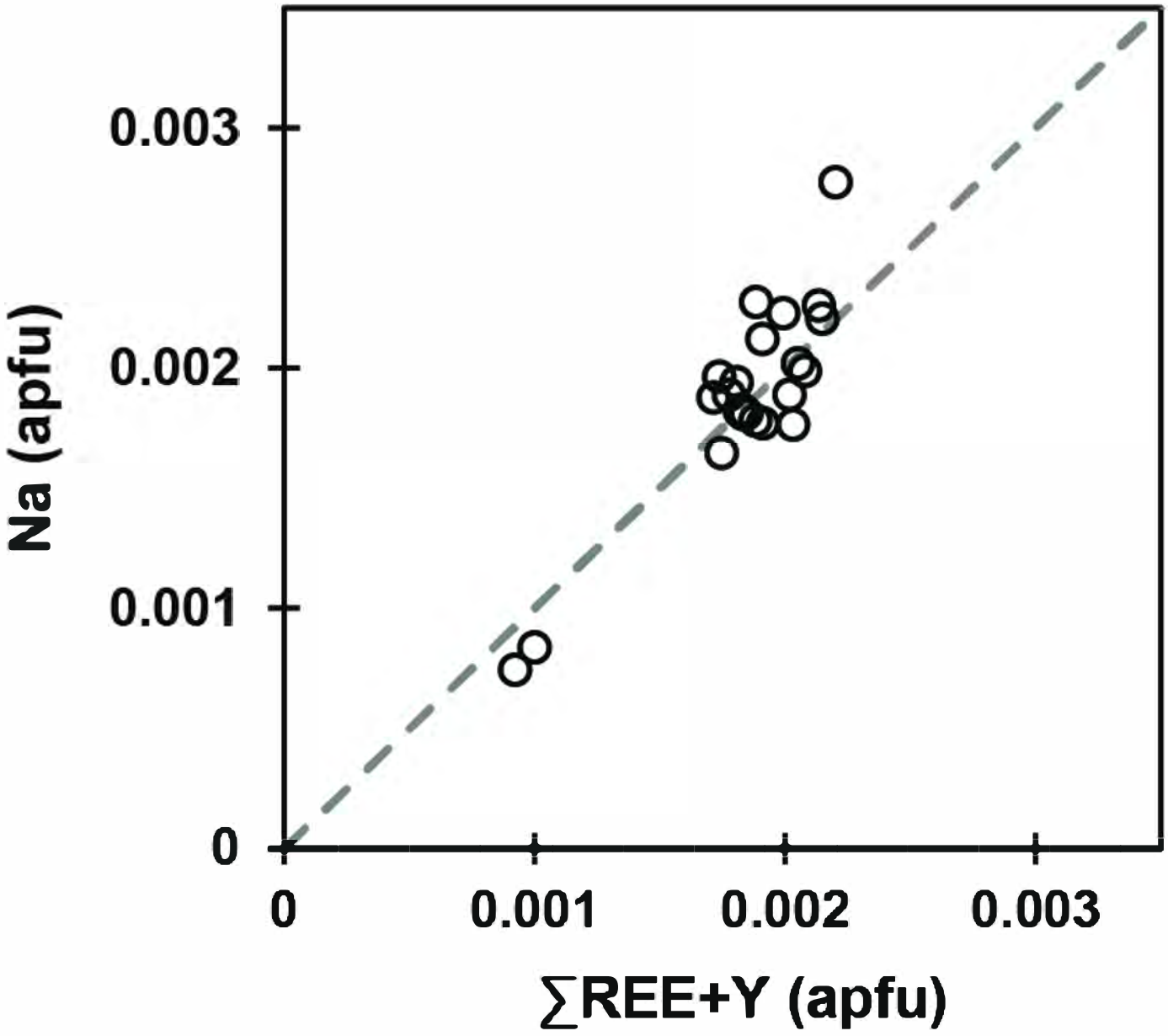

This is the peer-reviewed, final accepted version for American Mineralogist, published by the Mineralogical Society of America.
The published version is subject to change. Cite as Authors (Year) Title. American Mineralogist, in press.
DOI: https://doi.org/10.2138/am-2022-8345. http://www.minsocam.org/

Figure 9